V. Motta, A. Guardone, G. Quaranta
Influence of Airfoil Thickness on Unsteady Aerodynamic Loads on Pitching Airfoils
Journal of Fluid Mechanics, Vol. 774, 2015, p. 460-487
doi:10.1017/jfm.2015.280

Influence of airfoil thickness on unsteady aerodynamic loads on pitching airfoils

Valentina Motta, Alberto Guardone, Giuseppe Quaranta †

Department of Aerospace Science and Technology, Politecnico di Milano
via La Masa 34, 20156, Milano, Italy

(Received ?; revised ?; accepted ?. - To be entered by editorial office)

The influence of the airfoil thickness on the aerodynamic loads is investigated numerically for harmonically pitching airfoils at low incidence, under the incompressible and inviscid flow approximation. Force coefficients obtained from finite volume unsteady simulations of symmetrical 4-digit NACA airfoils are found to depart from the linear Theodorsen's model of an oscillating flat plate. In particular, the value of the reduced frequency resulting in the inversion—from clockwise to counter-clockwise—of the lift/angle-of-attack hysteresis curve is found to increase with the airfoil thickness. Indeed, both the magnitude and direction of the velocity vector due to pitching over the airfoil surface, differ from their flat-plate values. During the upstroke, namely, nose-up rotation, phase, this results in a decrease (increase) of the normal velocity magnitude over the upper (lower) surface of the airfoil. The opposite occurs during the down-stroke phase. This is confirmed by comparing the computed pressure distribution to the flat-plate linear Küssner's model. Therefore, beyond the inversion frequency, the lift coefficient of a finite-thickness airfoil is higher during upstroke and lower during down-stroke than its flat-plate counterpart. A similar dependence is found also for the quarter-chord moment coefficient. Accordingly, a modification to the classical Theodorsen's model is proposed to take into account the effects of the airfoil thickness on unsteady loads. The new model is found to accurately predict the unsteady aerodynamics of thick symmetric and slightly cambered airfoil with a maximum thickness in the range 4-24%. The limits of the present inviscid-flow analysis are assessed by means of numerical simulation of high-Reynolds ($\mathrm{Re} = 10^6$) flows.

Key words: Oscillating airfoil; four-digit NACA airfoil; airfoil thickness; Theodorsen's model; Küssner's model; inversion frequency

1. Introduction

The accurate evaluation of the unsteady aerodynamic loads around aerodynamic lifting bodies is of paramount importance in the determination of dynamic structural loads and aeroelastic stability in fixed- and rotary-wing aircraft, turbo-machinery and wind turbines. An accurate prediction of unsteady loads is also mandatory to evaluate the propulsive efficiency of flapping motion (see Garrick 1936; Freymuth 1988; Anderson *et al.* 1998) and to design load-alleviation devices (e.g. Kinzel *et al.* 2010). To understand all the implications of unsteadiness in the design process, it is necessary to achieve a deep knowledge into the theoretical fundamentals of unsteady flows and in particular of periodic motions.

† Email address for correspondence: giuseppe.quaranta@polimi.it

A large number of studies have been carried out to investigate the complex aerodynamics of airfoils in unsteady motion in different flow regimes. Kurosaka (1974) applied the linearized theory to the prediction of unsteady loads around airfoils oscillating at high reduced frequencies in supersonic flows. The dynamic loading over airfoil at low Reynolds number (up to 40 000) and in the incompressible limit was studied by e.g. Anderson *et al.* (1998), that observed peculiar flow field features, including so-called leading edge vortices and large-scale vortical structure in the wake. Baik *et al.* (2012) successfully compared experimental results to linear theory predictions in these conditions, which are relevant to the understating of the propulsion of fish and cetaceans and of insect flight. In particular, Uldrick & Siekmann (1964) investigated the effect of the airfoil thickness in swimming motion. At a larger angle of attack, so-called dynamic stall is possibly observed, see for example Panda & Zaman (1994). More recently, boundary layer transition and separation was studied experimentally by Lee & Gerontakos (2004) at $\mathrm{Re} = 135\,000$ for an oscillating NACA 0012 airfoil. High reduced frequency effects were measured for the NACA 0012 airfoil at $\mathrm{Re} = 12\,600$ by Bohl & Koochesfahani (2009). The reader is referred to the review of McCroskey (1982) for further details.

Physical models of different complexity have been proposed and validated through experiments and, more recently, by numerical simulations. The cornerstone models for unsteady aerodynamics were developed by Wagner (1925) in the time domain, and by Theodorsen (1935) for unsteady aerodynamic forces in the frequency domain. Relevant contributions to the field were given by e.g. Küssner (1936); Cicala (1936). Garrick (1938) demonstrated the equivalence between the Theodorsen's frequency domain function and the indicial response function developed by Wagner for the transient response of an impulsively started airfoil.

Most mathematical models derive from the small perturbation hypothesis, which is justified by the fact that the surface of aerodynamic lifting bodies can be approximated by the corresponding lifting flat-plate with zero thickness (see Bisplinghoff *et al.* 1955, Chapter 5). In accordance with the small perturbation hypothesis, the aerodynamic solution was obtained by Wagner (1925) and Theodorsen (1935) as a linear combination of elementary solutions corresponding to the separate contributions of the body angle of attack, camber and thickness distribution, under the further assumption that the coupling among these terms results is negligible. In particular, by using conformal mapping techniques, Theodorsen derived the analytical expression of the unsteady lift of a two-dimensional flat-plate moving in an inviscid incompressible flow, written in terms of three contributions: quasi-steady aerodynamics, the so-called added mass, and the wake unsteady contribution. Küssner & Schwarz (1941) were able to obtain the pressure distribution along the chord for an arbitrary spatial and temporal distribution of the velocity boundary condition on the airfoil, thus opening the way to the possibility of studying variable shape airfoils (see e.g. Gennaretti *et al.* 2013). Starting from these seminal works several authors developed more complex models to account for e.g. the fluid compressibility (see Fung 1955; Bisplinghoff *et al.* 1955, for extensive reviews). These models, with slight modifications, are currently being successfully applied to fixed-wing (see Bisplinghoff *et al.* 1955; Fung 1955) and rotary-wing (see Johnson 1980; Leishman 2006) aircraft design.

Extensions of the Theodorsen's theory were proposed to keep into account the effect of airfoil thickness of interest in the present work. These research activities were motivated by the limits of the linearity assumption and by the fact that the thin-airfoil theory exploited by Theodorsen is clearly unreliable in the airfoil nose region (see Barger 1975). Küssner (1960) developed a very elegant mathematical theory to account for the effect of the finite airfoil thickness. By resorting to conformal mapping techniques, Küssner

computed a set of modified Theodorsen's functions for Joukowsky airfoils. McCroskey (1973) developed a formulation for airfoils in unsteady motion, starting from the thin-airfoil theory, but keeping into account also the thickness and the camber, to evaluate the pressure distribution. The boundary velocity was expressed as the sum of three contributions. The camber and the thickness contributions are coincident with those obtained from the steady-flow theory (see e.g. Abbott & von Doenhoff 1949). The third term, which is a function of the angle of attack, accounts for the flow unsteadiness. The unsteady term depends on the ratio between the unsteady and the quasi-steady solution for a flat-plate. While being an extension of the Theodorsen's approach, in McCroskey (1973) the effects of unsteadiness are still restricted to the contribution of the angle of attack only.

Goldstein & Atassi (1976) showed that the effects of thickness, camber and angle of attack cannot simply be superimposed for the computation of the response of an airfoil to an incident gust. They developed a second order approximation taking into account the effect of the distortion of the incident disturbance that lead to a complex analytical expression for the unsteady lift, but in their analysis the effect of thickness on the unsteady lift was neglected because, according to the authors themselves, the "airfoil thickness probably has only an unimportant influence on the unsteady lift". A second order expansion was developed by Van Dyke (1953) for an oscillating airfoil in a supersonic flow. Glegg & Davenport (2009) developed a theory based on conformal mapping and Blasius theorem to evaluate the unsteady loading of an arbitrary thickness airfoil determined by an airfoil vortex interaction showing significant effects due to thickness.

The availability of computational fluid dynamics (CFD) tools, ousted almost completely the analytical formulations, also due to the high degree of complexity reached by the latter (see Goldstein & Atassi 1976). Several panel methods to compute numerically the unsteady incompressible potential flow around a moving airfoil are presented in the textbook by Katz & Plotkin (1991). A more refined approach capable of taking into account also compressibility effects was proposed by Morino (1974); Morino *et al.* (1975). As the computational power increased, numerical simulations based on e.g. the finite volume or finite elements discretization of the Euler of Reynolds–Averaged Navier–Stokes (RANS) equations, were used to study unsteady aerodynamic phenomena. Notwithstanding the advantages related to the use of a more complete physical model, several aspects may affect the reliability of numerical results, including the influence of the grid resolution or of the time integration scheme.

The understanding of the influence of airfoil thickness on the unsteady aerodynamic loads is still unsatisfactory, though the capability of predicting the aerodynamic loads in these conditions is of paramount importance in e.g. fixed- and rotary-wing design. The goal of the present paper is to provide a comprehensive description, under both a qualitative and a quantitative point of view, of the aerodynamic loads dependence on the airfoil thickness for small amplitude oscillations and in the low Mach limit. In these conditions, a linear and incompressible behavior can be expected. A CFD solver for RANS/Euler's equations is used to compute the aerodynamic flow-field to avoid the derivation of a complex analytical or semi-analytical solution of the potential problem.

In §2, the well-known linear theory results for oscillating airfoils are recalled, to underline the interplay between the airfoil thickness and the boundary conditions of the potential problem at the body interface. In §3 a brief overview of the considered computational model is given and its suitability for the problem under study is assessed. In §4, the results of the numerical simulation for symmetrical four-digit NACA airfoils are presented and an explanation of the dependence of aerodynamic loads on the airfoil thickness is provided. In §5 a modification to the flat-plate Theodorsen model is proposed,

which accounts for the thickness effects in the computation of the unsteady aerodynamic loads. Significant improvements with respect to the classical Theodorsen's formulation in computing the hysteresis cycles of finite thickness and slightly cambered airfoils are pointed out. In §6, final remarks and comments are given.

2. Review of linear theory for oscillating airfoils

The classical Theodorsen's linear theory for plunging and pitching airfoils, derives from the hypothesis of irrotational and incompressible flow. Under these assumptions, the point-wise value of the velocity vector $\boldsymbol{V}(\boldsymbol{x},t)$ is written as the sum of the constant free-stream velocity U_∞ (the x-axis is parallel to the free-stream velocity) and the perturbation velocity $\boldsymbol{v}(\boldsymbol{x},t)$, i.e. $\boldsymbol{V}(\boldsymbol{x},t) = U_\infty\hat{\boldsymbol{\imath}} + \boldsymbol{v}(\boldsymbol{x},t)$, where $\hat{\boldsymbol{\imath}}$ is the x-axis unit vector. The perturbation velocity is the gradient of a scalar function $\varphi(\boldsymbol{x},t)$ termed the perturbation potential, i.e. $\boldsymbol{v}(\boldsymbol{x},t) = \boldsymbol{\nabla}\varphi(\boldsymbol{x},t)$. In the linear theory, the perturbation velocity is assumed to be small with respect to the free-stream velocity, namely $|\boldsymbol{v}|/U_\infty \ll 1$. By combining the velocity potential definition and the continuity equation for incompressible flows, the well-known Laplace equation is obtained as

$$\nabla^2\varphi = 0, \tag{2.1}$$

which is to be made complete by suitable initial and boundary conditions.

At the body surface, the boundary condition is the well-known impermeability or slip condition, namely, $\boldsymbol{V}\cdot\boldsymbol{n} = \boldsymbol{v}_\mathrm{B}\cdot\boldsymbol{n}$, with $\boldsymbol{v}_\mathrm{B}$ local velocity of the solid surface. In terms of velocity potentials, the boundary condition is written as a Neumann condition as follows (see Katz & Plotkin 1991, Chapter 2)

$$\frac{\partial\varphi}{\partial n} = \left(\boldsymbol{v}_\mathrm{B} - U_\infty\hat{\boldsymbol{\imath}}\right)\cdot\boldsymbol{n}, \tag{2.2}$$

where $\boldsymbol{n}$ is the normal unit vector from the body surface and $\partial/\partial n = \boldsymbol{n}\cdot\boldsymbol{\nabla}$.

Sufficiently far from the airfoil, the so-called boundary condition at infinity is enforced,

$$\lim_{r\to\infty}\boldsymbol{v}(r) = o(r^{-1})$$

with r distance from the airfoil.

The boundary conditions along the wake are obtained by imposing the conservation of mass and momentum across the surface of discontinuity as

$$\Delta\left(\frac{\partial\varphi}{\partial n}\right) = 0$$
$$\Delta\varphi(\boldsymbol{x}_\mathrm{W},t) = \Delta\varphi(\boldsymbol{x}_\mathrm{TE},t-t_c),$$

where the symbol Δ indicates the difference between the two sides of the wake, $\boldsymbol{x}_\mathrm{TE}$ is the coordinate vector of the trailing edge, t_c is the convection time and the wake is described by the function $\boldsymbol{x} = \boldsymbol{x}_\mathrm{W}(s,t)$, with s curvilinear coordinates along the wake. At the trailing edge, one also has to explicitly impose the well known Kutta condition (see Morino 2003, pp. 1213–1214). It is not obvious that the Kutta condition for steady flows could be extended to unsteady flows as well. Experimental studies indicated that in fact the streamlines do not leave parallel to the trailing edge at reduced frequencies above 0.6 (Archibald 1975, see). However, for small-amplitude oscillations the pressure distribution and the lift are not affected significantly, so for practical purposes the unsteady Kutta condition is equivalent to the steady one, fixing the rear stagnation line to start at the trailing edge (see Katz & Plotkin 1991, Chapter 13, pp. 476–479).

From the potential equation (2.1), it is apparent that at larger times, when the transitory regime from initial conditions can be assumed to be terminated, the flow unsteadiness and possible non-linear terms can be introduced only by the displacement of the solid boundary, as duly detailed in the next section.

2.1. *Boundary conditions at the airfoil surface*

In the present section, the boundary condition at the body surface (2.2) is discussed. For simplicity, we start by considering the airfoil upper surface. The coordinate vector of each point along the upper surface is given by

$$\boldsymbol{\sigma}(s,t) = \boldsymbol{\sigma}_{\rm ca}(s) + \boldsymbol{\sigma}_{\rm th}(s) + \boldsymbol{\sigma}_{\rm ds}(s,t) = \boldsymbol{\sigma}_{\rm st}(s) + \boldsymbol{\sigma}_{\rm ds}(s,t), \tag{2.3}$$

where s is the curvilinear coordinate and where the flow direction is aligned with the x coordinate axis. The initial shape of the airfoil $\boldsymbol{\sigma}_{\rm st}$ at $t = 0$ is expressed as the sum of two terms: the mean line camber $\boldsymbol{\sigma}_{\rm ca}$ and the thickness $\boldsymbol{\sigma}_{\rm th}$. The quantity $\boldsymbol{\sigma}_{\rm ds}$ is the local surface displacement due to the airfoil motion.

The normal outward vector along the airfoil surface reads

$$\boldsymbol{n}(s,t) = -\frac{\partial \boldsymbol{\sigma}(s,t)}{\partial s} \times \hat{\boldsymbol{k}} = \boldsymbol{n}_{\rm st}(s) + \boldsymbol{n}_{\rm ds}(s,t), \tag{2.4}$$

where $\hat{\boldsymbol{k}}$ is the unit vector of the z-axis normal to the airfoil plane. The normal unit vector $\hat{\boldsymbol{n}}$ therefore reads

$$\hat{\boldsymbol{n}}(s,t) = \frac{\boldsymbol{n}}{|\boldsymbol{n}|} = \frac{\boldsymbol{n}_{\rm st} + \boldsymbol{n}_{\rm ds}}{|\boldsymbol{n}_{\rm st} + \boldsymbol{n}_{\rm ds}|}. \tag{2.5}$$

The modulus of the normal vector $\boldsymbol{n}$ is

$$\begin{aligned} |\boldsymbol{n}_{\rm st} + \boldsymbol{n}_{\rm ds}| &= \sqrt{|\boldsymbol{n}_{\rm st}|^2 + |\boldsymbol{n}_{\rm ds}|^2 + 2\,\boldsymbol{n}_{\rm st}\cdot\boldsymbol{n}_{\rm ds}} \\ &= |\boldsymbol{n}_{\rm st}| \sqrt{1 + 2\,\frac{\boldsymbol{n}_{\rm st}\cdot\boldsymbol{n}_{\rm ds}}{|\boldsymbol{n}_{\rm st}|^2} + \frac{|\boldsymbol{n}_{\rm ds}|^2}{|\boldsymbol{n}_{\rm st}|^2}} \\ &\simeq |\boldsymbol{n}_{\rm st}| \left[1 - \frac{\boldsymbol{n}_{\rm st}\cdot\boldsymbol{n}_{\rm ds}}{|\boldsymbol{n}_{\rm st}|^2} - \frac{1}{2}\frac{|\boldsymbol{n}_{\rm ds}|^2}{|\boldsymbol{n}_{\rm st}|^2}\right]^{-1} \end{aligned}$$

where in the last relation, the expansion $(1+\epsilon)^{1/2} \simeq (1-\epsilon/2)^{-1}$, valid for $\epsilon \ll 1$, is used. Namely, ϵ is defined as

$$\epsilon = 2\,\frac{\boldsymbol{n}_{\rm st}\cdot\boldsymbol{n}_{\rm ds}}{|\boldsymbol{n}_{\rm st}|^2} + \frac{|\boldsymbol{n}_{\rm ds}|^2}{|\boldsymbol{n}_{\rm st}|^2} \tag{2.6}$$

By considering only the first order displacement terms in (2.5), the linearized form of the normal unit vector reads

$$\hat{\boldsymbol{n}} \simeq \frac{\boldsymbol{n}_{\rm st} + \boldsymbol{n}_{\rm ds}}{|\boldsymbol{n}_{\rm st}|}\left(1 - \frac{\boldsymbol{n}_{\rm st}\cdot\boldsymbol{n}_{\rm ds}}{|\boldsymbol{n}_{\rm st}|^2}\right) \simeq \frac{\boldsymbol{n}_{\rm ds}}{|\boldsymbol{n}_{\rm st}|} + \left(1 - \frac{\boldsymbol{n}_{\rm ds}\cdot\boldsymbol{n}_{\rm st}}{|\boldsymbol{n}_{\rm st}|^2}\right)\hat{\boldsymbol{n}}_{\rm st}. \tag{2.7}$$

where in the last expression the second order term $\boldsymbol{n}_{\rm ds}(\boldsymbol{n}_{\rm ds}\cdot\boldsymbol{n}_{\rm ds})$ is neglected.

The expression (2.7) of the normal unit vector is now used to compute the normal component of the body displacement velocity as

$$\boldsymbol{v}_{\rm B}\cdot\hat{\boldsymbol{n}} = -\frac{\partial\boldsymbol{\sigma}}{\partial t}\cdot\left(\frac{\partial\boldsymbol{\sigma}}{\partial s}\times\hat{\boldsymbol{k}}\right) \simeq -\frac{\partial\boldsymbol{\sigma}_{\rm ds}}{\partial t}\cdot\hat{\boldsymbol{n}}, \tag{2.8}$$

where the velocity of the body is expressed in terms of the body displacement as $\boldsymbol{v}_{\rm B} = \partial\boldsymbol{\sigma}/\partial t = \partial\boldsymbol{\sigma}_{\rm ds}/\partial t$. By substituting (2.8) and the fluid velocity $\boldsymbol{V} = U_\infty\,\hat{\boldsymbol{\imath}} + \boldsymbol{\nabla}\varphi$, into the

boundary condition (2.2) one obtains

$$\begin{aligned}\frac{1}{U_\infty}\frac{\partial\varphi}{\partial n} &= -\hat{\boldsymbol{n}}\cdot\hat{\boldsymbol{i}} + \frac{1}{U_\infty}\frac{\partial\boldsymbol{\sigma}_{\rm ds}}{\partial t}\cdot\hat{\boldsymbol{n}} \\ &= -\left[\frac{\boldsymbol{n}_{\rm ds}}{|\boldsymbol{n}_{\rm st}|} + \left(1 - \frac{\boldsymbol{n}_{\rm ds}\cdot\boldsymbol{n}_{\rm st}}{|\boldsymbol{n}_{\rm st}|^2}\right)\hat{\boldsymbol{n}}_{\rm st}\right]\cdot\hat{\boldsymbol{i}} + \frac{1}{U_\infty}\frac{\partial\boldsymbol{\sigma}_{\rm ds}}{\partial t}\cdot\hat{\boldsymbol{n}}_{\rm st} \\ &= \theta_{\rm st}(s) + \theta_{\rm ge}(s,t) + \theta_{\rm ki}(s,t), \end{aligned} \tag{2.9}$$

where the following definitions were introduced

$$\theta_{\rm st}(s) = -\hat{\boldsymbol{n}}_{\rm st}\cdot\hat{\boldsymbol{i}}, \tag{2.10}$$

$$\theta_{\rm ge}(s,t) = -\left[\frac{\boldsymbol{n}_{\rm ds}}{|\boldsymbol{n}_{\rm st}|} - \frac{\boldsymbol{n}_{\rm ds}\cdot\boldsymbol{n}_{\rm st}}{|\boldsymbol{n}_{\rm st}|^2}\hat{\boldsymbol{n}}_{\rm st}\right]\cdot\hat{\boldsymbol{i}}, \tag{2.11}$$

$$\theta_{\rm ki}(s,t) = \frac{1}{U_\infty}\frac{\partial\boldsymbol{n}_{\rm ds}}{\partial t}\cdot\hat{\boldsymbol{n}}_{\rm st} \tag{2.12}$$

The function $\theta_{\rm st}$ is the local angle of attack at $t=0$, $\theta_{\rm ge}$ is the geometric angle of attack due to the airfoil displacement, and $\theta_{\rm ki}$ is the kinematic angle of attack, resulting from the body velocity. Notice that $\theta_{\rm st}$ is constant, whereas $\theta_{\rm ge}$ and $\theta_{\rm ki}$ depend on time.

If only plunge and pitch movement around the point $(x_0, 0)$ are considered, for small angles of rotation the displacement vector $\boldsymbol{\sigma}_{\rm ds}$ reads

$$\boldsymbol{\sigma}_{\rm ds} = \begin{Bmatrix}0\\1\end{Bmatrix} h(t) + \begin{Bmatrix}-\boldsymbol{\sigma}_{\rm st}^{(y)}\\ x - x_0\end{Bmatrix}\alpha(t), \tag{2.13}$$

where the superscript (y) indicates the y-component of a vector, $h = h(t)$ is the y displacement due to the plunge motion, $\alpha = \alpha(t)$ is the angle of attack. For small airfoil displacements, $s \sim x$ and one has

$$\frac{\partial\boldsymbol{\sigma}_{\rm st}}{\partial s} = \frac{\partial\boldsymbol{\sigma}_{\rm st}}{\partial x}\frac{\partial x}{\partial s} + \frac{\partial\boldsymbol{\sigma}_{\rm st}}{\partial y}\frac{\partial y}{\partial s} \simeq \frac{\partial\boldsymbol{\sigma}_{\rm st}}{\partial x}.$$

Moreover, according to the hypothesis of small perturbation that is usually valid for standard airfoils outside the nose area, one also has

$$\frac{\partial\boldsymbol{\sigma}_{\rm ca}^{(y)}}{\partial s} \ll 1,\ \frac{\partial\boldsymbol{\sigma}_{\rm th}^{(y)}}{\partial s} \ll 1 \quad\Rightarrow\quad \frac{\partial\boldsymbol{\sigma}_{\rm st}^{(x)}}{\partial x} \simeq 1,\ \frac{\partial\boldsymbol{\sigma}_{\rm st}^{(y)}}{\partial x} \ll 1.$$

Therefore, from definition (2.4), one immediately obtains

$$\boldsymbol{n}_{\rm st}(s) = \begin{Bmatrix} -\dfrac{\partial\boldsymbol{\sigma}_{\rm st}^{(y)}}{\partial x} \\ 1 \end{Bmatrix}, \quad |\boldsymbol{n}_{\rm st}| \simeq 1, \qquad \boldsymbol{n}_{\rm ds}(s,t) = \begin{Bmatrix} 1 \\ -\dfrac{\partial\boldsymbol{\sigma}_{\rm st}^{(y)}}{\partial x} \end{Bmatrix}\alpha(t), \quad |\boldsymbol{n}_{\rm ds}| \simeq \alpha(t) \tag{2.14}$$

By substituting the above expressions into (2.10) and (2.11), the sum of the initial and geometric angle of attack reads

$$\theta_{\rm st} + \theta_{\rm ge} = \frac{\partial\boldsymbol{\sigma}_{\rm st}^{(y)}}{\partial x} + \left[1 + \left(\frac{\partial\boldsymbol{\sigma}_{\rm st}^{(y)}}{\partial x}\right)^2\right]\alpha(t) \simeq \frac{\partial\boldsymbol{\sigma}_{\rm st}^{(y)}}{\partial x} + \alpha(t), \tag{2.15}$$

where only first-order terms have been retained. It is remarkable that, according to the small perturbation theory, the unsteady contribution to the sum of the initial and geometric angle of attack does not depend on the airfoil thickness. The linearized body

velocity vector is

$$\frac{\partial \boldsymbol{\sigma}_{\rm ds}}{\partial t} = \begin{Bmatrix} 0 \\ 1 \end{Bmatrix} \frac{\mathrm{d}\, h(t)}{\mathrm{d}\, t} + \begin{Bmatrix} -\boldsymbol{\sigma}_{\rm st}^{(y)} \\ x - x_0 \end{Bmatrix} \frac{\mathrm{d}\, \alpha(t)}{\mathrm{d}\, t}, \tag{2.16}$$

and therefore the kinematic angle of attack reads

$$\theta_{\rm ki} = \frac{1}{U_\infty} \left[\frac{\mathrm{d}\, h(t)}{\mathrm{d}\, t} - (x - x_0) \frac{\mathrm{d}\, \alpha(t)}{\mathrm{d}\, t} + \boldsymbol{\sigma}_{\rm st}^{(y)} \frac{\partial \boldsymbol{\sigma}_{\rm st}^{(y)}}{\partial x} \frac{\mathrm{d}\, \alpha(t)}{\mathrm{d}\, t} \right]. \tag{2.17}$$

Therefore, under the small perturbation hypothesis, the boundary condition (2.2) can be written as

$$\frac{\partial \varphi}{\partial n} = U_\infty \frac{\partial \boldsymbol{\sigma}_{\rm st}^{(y)}}{\partial x} + U_\infty \alpha(t) + \frac{\mathrm{d}\, h(t)}{\mathrm{d}\, t} - (x - x_0) \frac{\mathrm{d}\, \alpha(t)}{\mathrm{d}\, t} + \boldsymbol{\sigma}_{\rm st}^{(y)} \frac{\partial \boldsymbol{\sigma}_{\rm st}^{(y)}}{\partial x} \frac{\mathrm{d}\, \alpha(t)}{\mathrm{d}\, t}. \tag{2.18}$$

The difference of the normal derivative of the potential between the upper and lower surface of the airfoil, namely,

$$\Delta \left(\frac{\partial \varphi}{\partial n} \right) = U_\infty \, \Delta \big[\theta_{\rm st}(s) + \theta_{\rm ge}(s,t) + \theta_{\rm ki}(s,t) \big]. \tag{2.19}$$

is now computed. By recalling that on the lower surface of the airfoil the boundary coordinates are given by $\boldsymbol{\sigma}^- = \boldsymbol{\sigma}_{\rm ca} - \boldsymbol{\sigma}_{\rm th} + \boldsymbol{\sigma}_{\rm ds}$, one immediately obtains

$$\tfrac{1}{2} \Delta \big[\theta_{\rm st}(s) + \theta_{\rm ge}(s,t) \big] = \frac{\partial \boldsymbol{\sigma}_{\rm ca}^{(y)}}{\partial x} + \alpha(t) \tag{2.20}$$

and the difference of the kinematic angle of attack is

$$\tfrac{1}{2} U_\infty \Delta \theta_{\rm ds}(s,t) = \frac{\mathrm{d}\, h(t)}{\mathrm{d}\, t} - (x - x_0) \frac{\mathrm{d}\, \alpha(t)}{\mathrm{d}\, t} + \boldsymbol{\sigma}_{\rm th}^{(y)} \left[\frac{\partial \boldsymbol{\sigma}_{\rm ca}^{(y)}}{\partial x} + \frac{\partial \boldsymbol{\sigma}_{\rm th}^{(y)}}{\partial x} \right] \frac{\mathrm{d}\, \alpha(t)}{\mathrm{d}\, t}. \tag{2.21}$$

In standard shape airfoil, one can usually assume

$$\frac{\partial \boldsymbol{\sigma}_{\rm ca}^{(y)}}{\partial x} \ll \frac{\partial \boldsymbol{\sigma}_{\rm th}^{(y)}}{\partial x} \tag{2.22}$$

and therefore, relation (2.19) simplifies to

$$\tfrac{1}{2} \Delta \left(\frac{\partial \varphi}{\partial n} \right) = U_\infty \frac{\partial \boldsymbol{\sigma}_{\rm th}^{(y)}}{\partial x} + U_\infty \alpha(t) + \frac{\mathrm{d}\, h(t)}{\mathrm{d}\, t} - (x - x_0) \frac{\mathrm{d}\, \alpha(t)}{\mathrm{d}\, t} + \boldsymbol{\sigma}_{\rm th}^{(y)} \frac{\partial \boldsymbol{\sigma}_{\rm th}^{(y)}}{\partial x} \frac{\mathrm{d}\, \alpha(t)}{\mathrm{d}\, t}. \tag{2.23}$$

By neglecting the thickness effects, namely, by assuming $\boldsymbol{\sigma}_{\rm th} \equiv \mathbf{0}$, Theodorsen (1931) derived the well-known model for an oscillating flat plate reported in §2.2, see also (Katz & Plotkin 1991). In deriving his model for the unsteady aerodynamic loads, McCroskey (1973) computed the camber and thickness velocity contributions using the steady theory. Moreover, he took into account the steady non-linear velocity contributions close to the airfoil leading edge and neglected the unsteady contribution from the thickness. To the authors knowledge, the last unsteady term in (2.18), which is identically zero for a flat plate, was neglected in all analytical and semi-analytical solutions of the potential flow equations, though its presence is fully justified within the small perturbation theory.

We conclude that, under the assumption (2.22), the potential difference across the airfoil contains an unsteady term that is proportional to the airfoil thickness and its first order spatial derivative, thus indicating that the airfoil thickness may produce a non-negligible contribution to the aerodynamic load within the small perturbation theory. While within the thin airfoil hypothesis, i.e. $\boldsymbol{\sigma}_{\rm th}^{(y)} \to 0$, the last term of (2.23) can be

neglected, for airfoils with finite thickness it may be possible that somewhere along the chord the term $\boldsymbol{\sigma}_{\rm th}^{(y)}\partial\boldsymbol{\sigma}_{\rm th}^{(y)}/\partial x$ may be comparable or even larger than $(x-x_0)$. This contribution was neglected in previous studies and it is the focus of the present analysis. It is remarkable that if the rotation center x_0 is close to the point of maximum airfoil thickness—as it is the case in most aerodynamic applications—the sign of $-(x-x_0)$ is equal to that of $\boldsymbol{\sigma}_{\rm th}^{(y)}\partial\boldsymbol{\sigma}_{\rm th}^{(y)}/\partial x$ and therefore the inclusion of the last term in (2.19) results in an increase of the modulus of the flat-plate contribution to the potential difference across the airfoil.

2.2. *Theodorsen's model for oscillating airfoils*

For later convenience, the main results of the (Theodorsen 1935) solution for a flat-plate ($\boldsymbol{\sigma}_{\rm ca}\equiv\boldsymbol{\sigma}_{\rm th}\equiv\boldsymbol{0}$) subject to harmonic motions composed by airfoil plunge and pitch, is briefly recalled. In the model, both the airfoil and the wake are represented by a vortex sheet, with the shed wake extending as a planar surface from the trailing edge downstream to infinity, i.e. , $\boldsymbol{x}_{\rm W}=(s,\boldsymbol{x}_{\rm TE}^{(y)}),\forall s>\boldsymbol{x}_{\rm TE}^{(x)},t>0$.

The solution is given by Theodorsen in terms of the transfer function between the forcing movements (plunge h and pitch α) and the aerodynamic response (lift and pitching moment) at a given reduced frequency $k=\omega b/U$, with ω oscillation frequency, as

$$C_L(k)=2\pi\alpha_0+\pi b\left[\frac{\ddot{h}}{U_\infty^2}+\frac{\dot{\alpha}}{U_\infty}-\frac{ba}{U_\infty^2}\ddot{\alpha}\right]+2\pi C(k)\left[\frac{\dot{h}}{U_\infty}+\alpha-\alpha_0+\frac{b}{U_\infty}\left(\frac{1}{2}-a\right)\dot{\alpha}\right], \tag{2.24}$$

for the lift coefficient C_L and

$$C_m(k)=-\frac{1}{2}\pi b\left[\frac{1}{2U_\infty^2}\ddot{h}+\frac{1}{U_\infty}\dot{\alpha}+\frac{b}{2U_\infty^2}\left(\frac{1}{4}-a\right)\ddot{\alpha}\right]. \tag{2.25}$$

for the moment coefficient C_m with the respect to the $c/4$ point, where α_0 is the static angle of attack. The parameter a is the position of the rotation center with respect to the mid-chord, made dimensionless with the semi-chord b.

The lift coefficient (2.24) is written as the sum of two terms. The first is the so-called non-circulatory part and corresponds to the added mass. It accounts for the pressure forces required to accelerate the fluid near the airfoil. The second term is called the circulatory part and it is multiplied by the complex Theodorsen's function $C(k)\in\mathbb{C}$. This term is in fact the sum of the quasi-steady lift:

$$C_{L_{\rm qs}}=2\pi\left[\frac{\dot{h}}{U_\infty}+\alpha+\frac{b}{U_\infty}\left(\frac{1}{2}-a\right)\dot{\alpha}\right]$$

and the lift attenuation due to the shedding of vorticity into the wake that is equal to $(1-C(k))C_{L_{\rm qs}}$. It is interesting to note that the moment coefficient with respect to $c/4$ does not depend on the circulatory part but only on the added mass effect. The complex function $C(k)$ is defined as

$$C(k)=\frac{H_1^{(2)}(k)}{H_1^{(2)}(k)+{\rm j}H_0^{(2)}(k)}, \tag{2.26}$$

where $H_1^{(2)}$ and $H_0^{(2)}$ are Hankel functions that involve Bessel's functions of the first and of the second kind (see Theodorsen 1935).

The C_L curve (2.24) as a function of the angle of attack α is shown in Figure 1 for three values of the reduced frequency k, namely, 0.1, 0.3 and 0.5, against their steady state

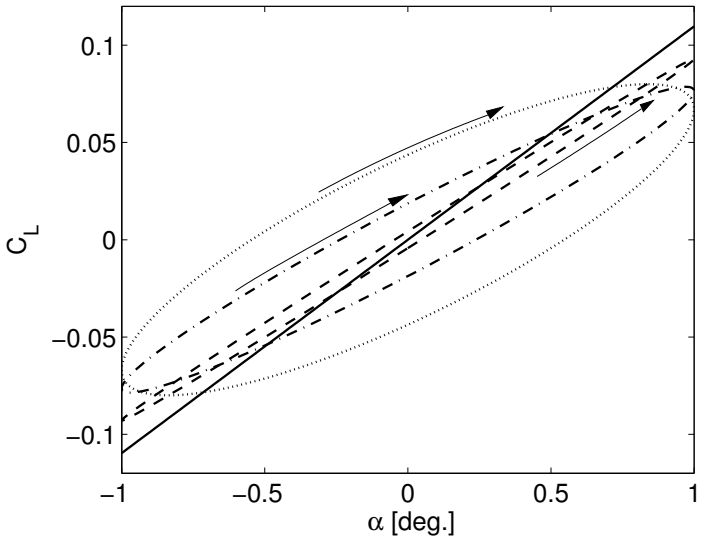

FIGURE 1. Lift coefficient curve due to a pitch oscillation for the steady case (continuous line) and the unsteady case at three different reduced frequencies: $k = 0.1$ dashed line, counter-clockwise; $k = 0.3$ dot-dashed line clockwise; $k = 0.5$ dotted line clockwise.

counterpart ($C(k) = 1$, $k = \omega = 0$). The curve in Figure 1 is drawn by recalling that the real part of $C_L(k)$ represents the portion of the harmonic load that oscillates in phase with the input, while the imaginary part represents the one that is in quadrature (i.e. 90 deg. delay). As is well known, a hysteresis cycle is observed, together with a reduction of the maximum value of the lift coefficient with increasing reduced frequencies. Figure 1 also shows that for low reduced frequency values, the orientation of the cycle is counter-clockwise, while for higher frequencies it is clockwise. This effect can be noticed more clearly by considering the diagrams of the magnitude and the phase of the lift coefficient in (2.24), shown in Figures 2(a) and 2(b). Notice that the lift coefficient magnitude depicted in Figure 2(a) is normalized with respect to the amplitude of the input motion. Therefore, at $k = 0$, the modulus of the lift coefficient is expected to be equal to the slope of the C_L-α curve which, for a steady flat plate, is 2π. Figure 2(a) clearly shows that 2π is indeed the value of the lift magnitude at $k = 0$. At low reduced frequency the lift is rotating counter-clockwise (phase negative) due to the dominant action of the circulatory contribution. Instead, for higher reduced frequencies, the dominant apparent mass contribution, proportional to the airfoil acceleration, cause the anticipation (phase positive) of the lift. In particular, the phase curve, Figure 2(b), shows a change of slope followed by a point where the phase curve crosses the zero value at $k = 0.144$, which is referred to in the following as the *phase inversion* point. In this situation the amplitude of the hysteresis cycle is null. For larger values of k, the cycle orientation is clockwise.

By taking the above Theodorsen's result as the baseline, the effects of a non-zero airfoil thickness on the aerodynamic loads are assessed in the following sections for pitching movement only. To avoid the analytical or semi-analytical solution of the potential equation (2.1) with the boundary conditions (2.18), a finite volume CFD solver based on RANS/Euler's equation models is used to compute the aerodynamic loads, without introducing any undue simplification when compared to a wind tunnel test campaign. In

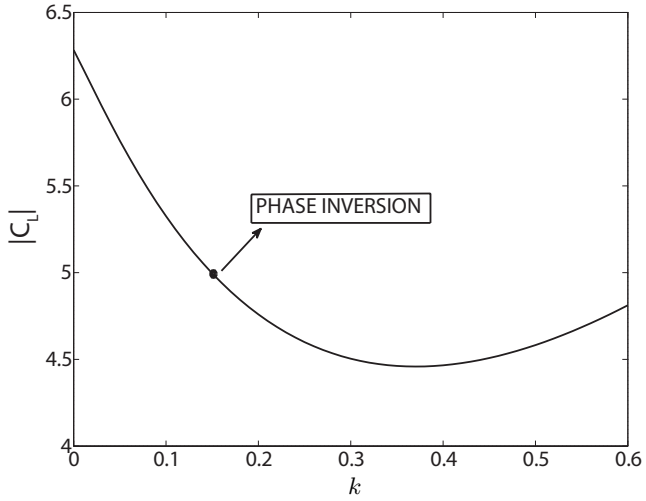

(a) Magnitude

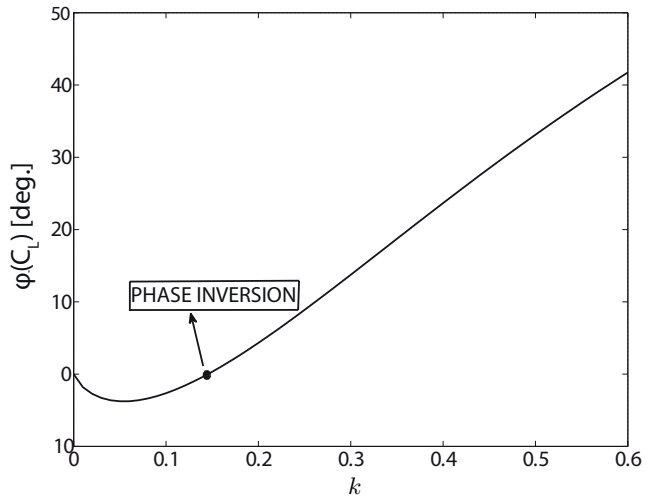

(b) Phase

FIGURE 2. Lift coefficient at various reduced frequencies for a unitary pitch oscillation.

§3, the solver capabilities in reproducing the flow of interest is assessed. In §4, numerical results are presented and discussed.

3. Numerical simulation of pitching airfoils

The numerical simulations for the unsteady oscillation of a pitching airfoil were carried out using the ROSITA flow solver (see Biava 2007), a finite volume Euler/RANS solver for moving, overset, multi-block grids. The equations of motion are discretized in space by means of a cell-centered finite-volume implementation of either the scheme of Roe (1981) or the one proposed by Jameson *et al.* (1981). Second order accuracy in space in smooth flow regions is obtained by MUSCL extrapolation using the modified version of the Van

Albada limiter introduced by Venkatakrishnan (see Venkatakrishnan & Mavriplis 1996). The viscous terms are computed by applying the Gauss theorem and using a centered approximation scheme. Time integration is carried out with a dual-time formulation, employing a second order backward differentiation formula (BDF) to approximate the time derivative and a fully unfactored implicit scheme in the pseudo-time. The generalized conjugate gradient (GCG), in conjunction with a block incomplete lower-upper preconditioner, is used to solve the resulting linear system. Details of the implementation can be found in Biava (2007), Drikakis *et al.* (2012) and Khier *et al.* (2012).

Unsteady computations were performed to simulate the behavior of a symmetrical airfoil pitching around its $c/4$ point (approximately the aerodynamic center of the airfoil). The general form of the harmonic law used in this case is

$$\alpha = \alpha_0 + \alpha_m \sin(\omega t), \tag{3.1}$$

where α_0 is the mean angle, α_m is the maximum magnitude of the oscillation and ω is the frequency. To assess the reliability of ROSITA unsteady solutions, a comparison of Theodorsen's model, numerical and experimental data was performed.

Figure 3(a) reports the lift hysteresis curves obtained for the NACA 0012 with $k = 0.4$, $\mathrm{Ma} = 0.1$, $\mathrm{Re} = 10^6$, $\alpha_0 = 0$ and $\alpha_m = 6.7$ deg. The experimental results for this case are reported by Halfman (1952), and were used as a benchmark for numerical computation by Lin *et al.* (2006). Viscous and inviscid fluid simulations were carried out with the ROSITA solver for comparison. The viscous fluid simulation required a finer grid ($[400+80]\times 70$ C-type structured mesh, with 400 elements over the airfoil, 80 elements along the wake and 70 elements in the normal directions), accounting for the boundary layer. In this case the Spalart & Allmaras (1994) turbulence model was used to represent the Reynolds stress tensor of the RANS. In the inviscid case it was possible to use a coarser grid ($[300+60]\times 40$ C-type structured mesh), hence reducing significantly the computational burden. The viscous results show a somewhat higher error, probably due to the still insufficient grid refinement. Since we are interested in investigating a phenomenon where viscosity is expected to have a limited impact, the inviscid set of equation was chosen to reduce the computational burden. Figure 3(b) shows how the Theodorsen's model does not match exactly the experimental hysteresis amplitude. The model of McCroskey (1973), including a steady-state correction for thickness effects, does not show significant improvements over the Theodorsen's model in reproducing the experimental results in this condition.

The difference of the pressure coefficient between the upper and lower side of the airfoil was computed for the same case. Figure 4 compares the results obtained by means of ROSITA with those obtained by using the formulation of Küssner & Schwarz (1941), which is based on the same approach used by Theodorsen but provides local pressure distributions, and the formulation presented by McCroskey (1973), which includes the effects of thickness in the reference flow. Some differences of the thin-airfoil solutions with respect to the CFD are visible not only in the nose area, where these are expected due to the flat-plate approximation, but also in the central part of the airfoil.

Results in figures 3 and 4 highlight that the Theodorsen and the McCroskey models show some errors in the prediction the aerodynamic loads for airfoils of finite thickness, both in terms of local distributions and integral coefficients. As a consequence, only the CFD code ROSITA is used in the following to quantify the thickness contribution.

A second numerical test at a higher Mach number was considered. The conditions were: $k = 0.0814$, $\mathrm{Ma} = 0.755$, $\alpha_0 = 0.016$ deg. $\alpha_m = 2.51$ deg. This test condition was taken as benchmark in the work by Venkatakrishnan & Mavriplis (1996) and are extracted from the report VV. AA. (1982). Figure 5 shows a good overlapping between ROSITA and

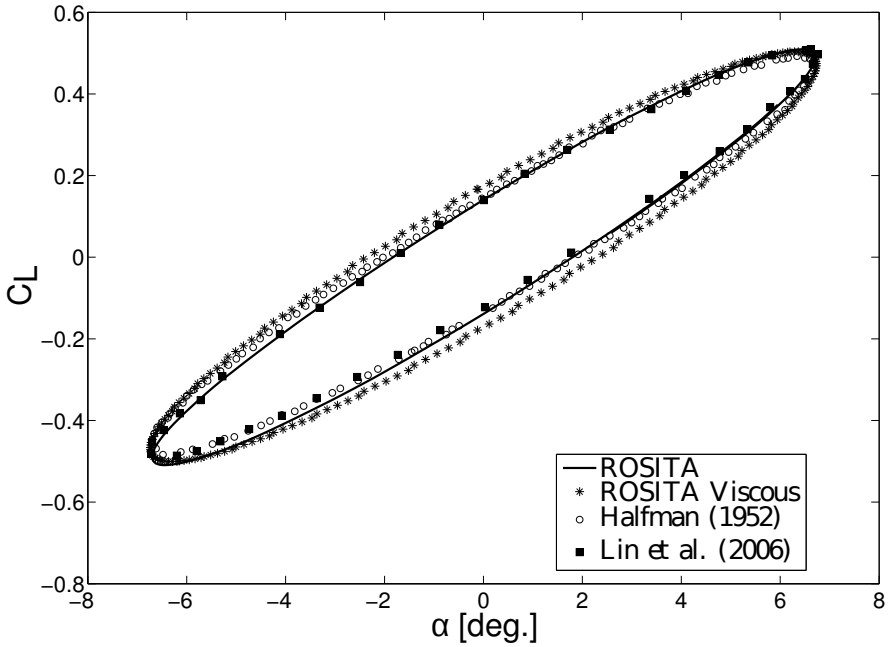

(a) Comparison with experiments of Halfman (1952) and numerical computations of Lin *et al.* (2006)

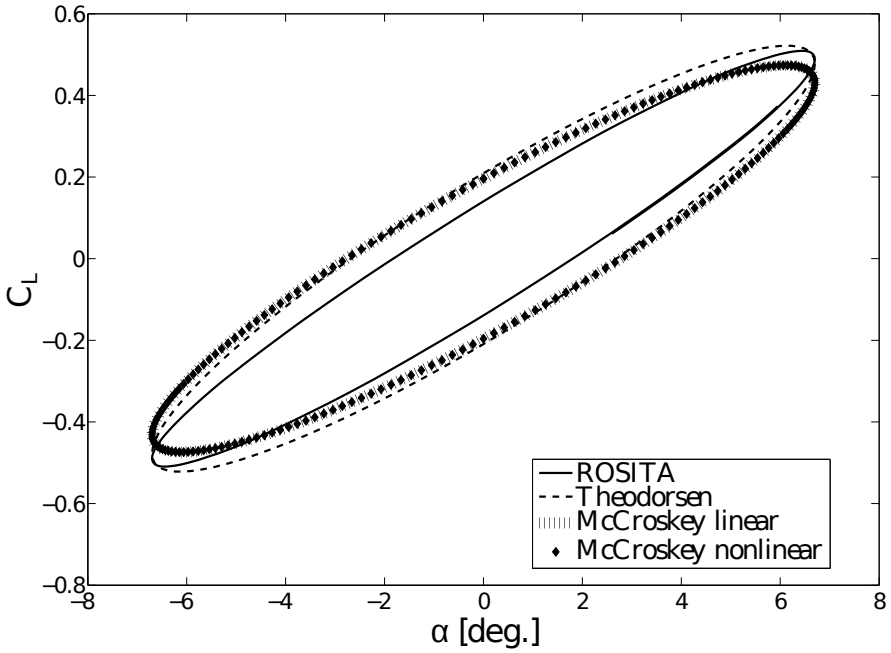

(b) Comparison with the analytical models of Theodorsen (1931) and McCroskey (1973)

FIGURE 3. Lift coefficient history for the NACA 0012 airfoil with $k = 0.4$, Ma $= 0.1$, Re $= 10^6$, $\alpha_0 = 0$ deg. and $\alpha_m = 6.7$ deg.

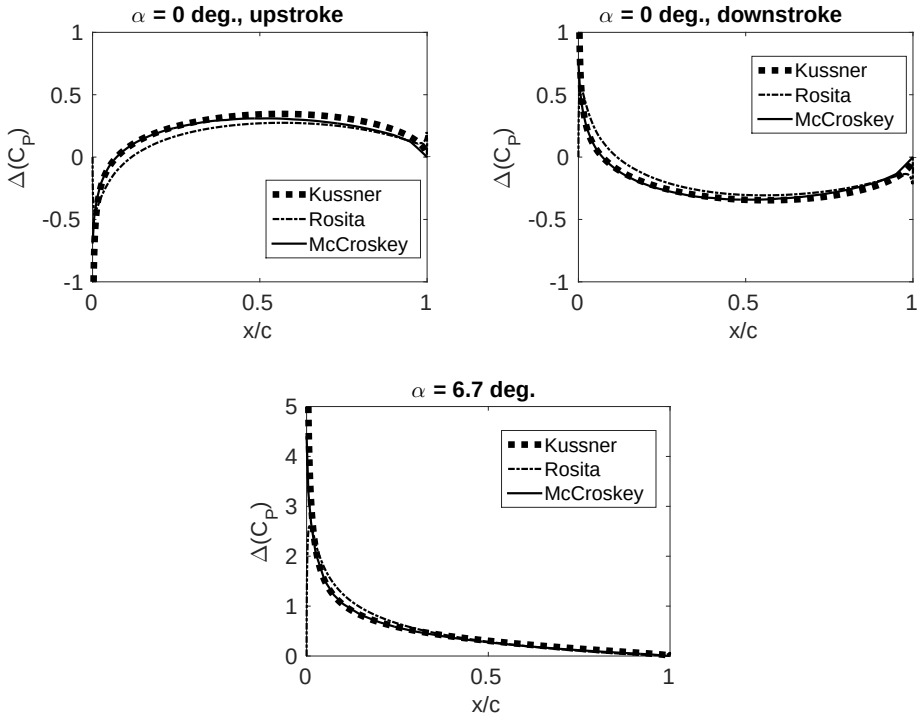

FIGURE 4. Difference of pressure coefficient between the upper and lower side of the airfoil for the NACA 0012 airfoil with $k = 0.4$, Ma $= 0.1$, Re $= 10^6$, $\alpha_0 = 0$ deg. and $\alpha_m = 6.7$ deg. Distributions at the $\alpha = 0$ (both upstroke and downstroke phase), maximum angle of attack.

C-type grids:	$[212 + 40] \times 28$, $[300 + 60] \times 40$, $[424 + 80] \times 56$
Time steps per period:	100, 200, 400
Reduced frequency k:	0.025, 0.01, 0.1

TABLE 1. Test matrix used to study the numerical convergence of the solution. All 27 combinations of the parameters were considered in the simulations in Figure 6.

Venkatakrishnan & Mavriplis (1996) computations. However, the accuracy with respect to the experimental data is poor in both cases, probably due to an offset in the mean angle of attack. Additionally, the hysteresis cycle resulting from the Theodorsen formulation is shown. As expected, this incompressible flat plate formulation fails in predicting the unsteady airloads, when not negligible compressibility effects are encountered.

The dependence of the numerical results on both the grid spacing Δx and the time step Δt is assessed for different reduced frequencies. Simulations were performed at all possible combinations of parameters reported in Table 1. Figure 6 shows the C_L amplitude and phase for the points listed in the test matrix computed for the NACA 0004 airfoil together with the Theodorsen's model curves. The continuous line is the baseline solution computed over a $[300 + 60] \times 40$ C-type structured mesh with 200 time steps for each period. The NACA 0004 was chosen due to the very low thickness (4%) which resembles Theodorsen's flat-plate model. Each symbol in figure 6 represents a simulation point. At low reduced frequency values, simulation results are more scattered, thus indicating a strong grid/time step dependence that is not observed at higher reduced

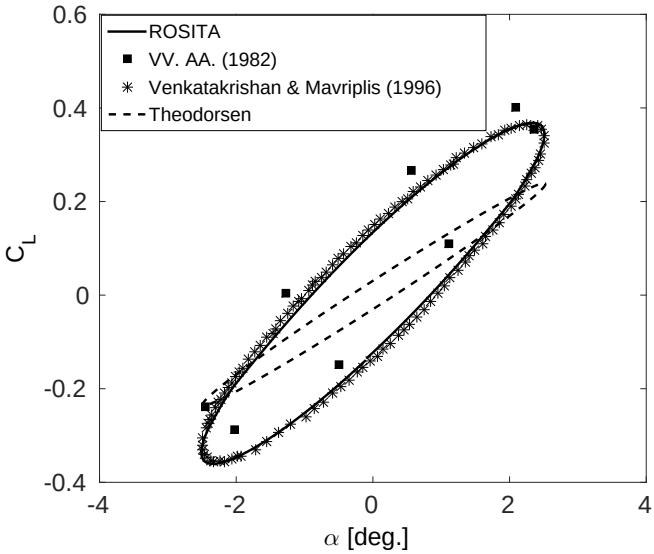

FIGURE 5. Lift coefficient history for the NACA 0012 airfoil with $k = 0.0814$, Ma $= 0.755$, $\alpha_0 = 0.016$ deg., $\alpha_m = 2.51$ degrees. Comparison between the present numerical results, the CFD results of Venkatakrishnan & Mavriplis (1996) and the experimental data of VV. AA. (1982). The hysteresis curve computed with the flat plate incompressible Theodorsen model is also represented.

frequencies. This is not surprising since, for $k \to 0$, Δt grows if the number of time samples per cycle is kept fixed, and consequently the integration error becomes larger at low reduced frequency. Numerical results are deemed to be satisfactory for the purposes of the present investigation, since they accurately reproduce the flat plate results at the frequencies of interest. The accuracy of the numerical simulations is confirmed by the C_L hysteresis curve shown in Figure 7, which is practically independent on the grid spacing and the time step.

4. Results and discussion

To investigate numerically the effect of the airfoil thickness on the loads, unsteady inviscid simulations were carried out for four symmetrical airfoils: NACA 0004, NACA 0012, NACA 0018 and NACA 0024 airfoil at different reduced frequencies. Therefore, the maximum thickness ranges from 4% to 24% of the airfoil chord. For each airfoil, a value of k between 0.01 and 0.75 was considered. The Mach number is Ma $= 0.117$, which corresponds to an almost incompressible flow. The mean angle of attack is $\alpha_0 = 0$ deg. and the oscillation amplitude is $\alpha_m = 1.0$ deg. In the following the results of few tests are discussed to expose the modification to unsteady loads induced by the airfoil thickness.

The results obtained at a reduced frequency below the phase inversion point ($k = 0.1$) are shown in Figure 8. The hysteresis curve of the NACA 0004 are almost indistinguishable from those computed using the Theodorsen's method. By increasing the airfoil thickness, the amplitude of the hysteresis cycle is increased. The opposite behavior is experienced for reduced frequencies above the phase inversion point, as shown in Figure 9. In this case the increase of thickness causes a reduction of the amplitude of the counter-clockwise hysteresis cycles. Several analyses have been performed by doubling

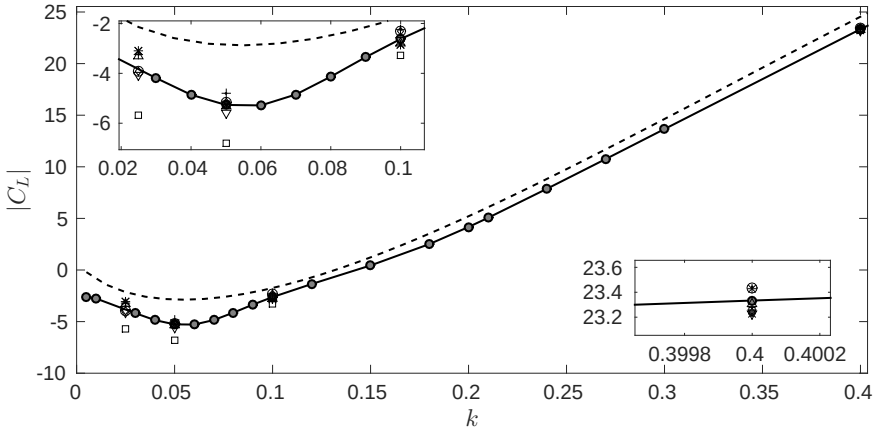

(a) Amplitude

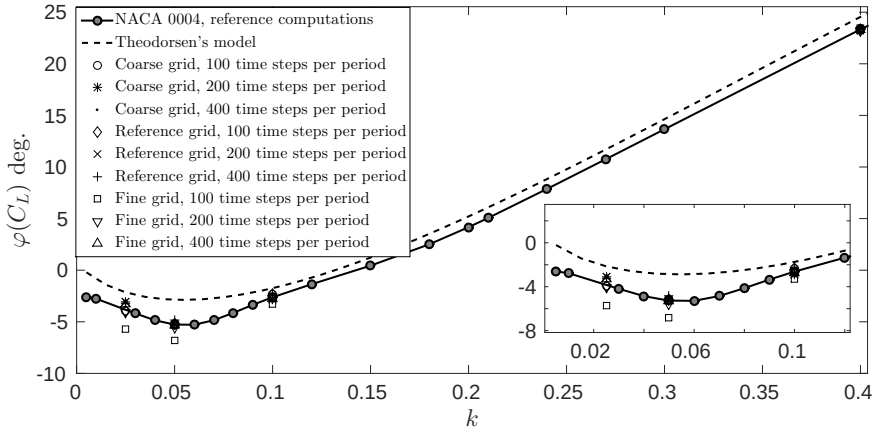

(b) Phase

FIGURE 6. Amplitude and phase of the C_L function for the NACA 0004 airfoil (—) against the prediction of the Theodorsen model (- - -). The empty markers correspond to results obtained for different grid resolutions and time steps per period (listed in Table 1). The filled circles indicate the reduced frequency computed using CFD.

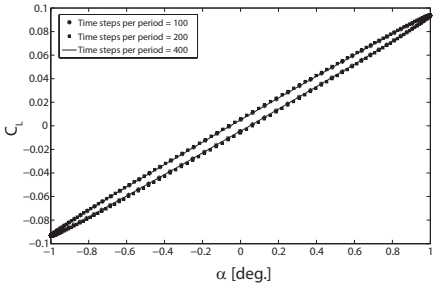

(a) Time convergence

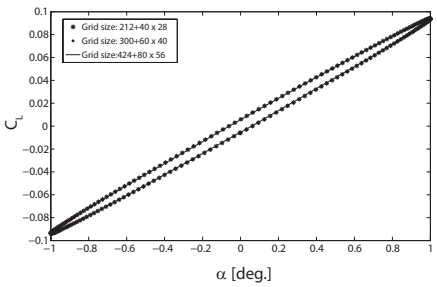

(b) Space convergence

FIGURE 7. Numerical convergence in the time domain for the NACA 0004 airfoil, $k = 0.1$.

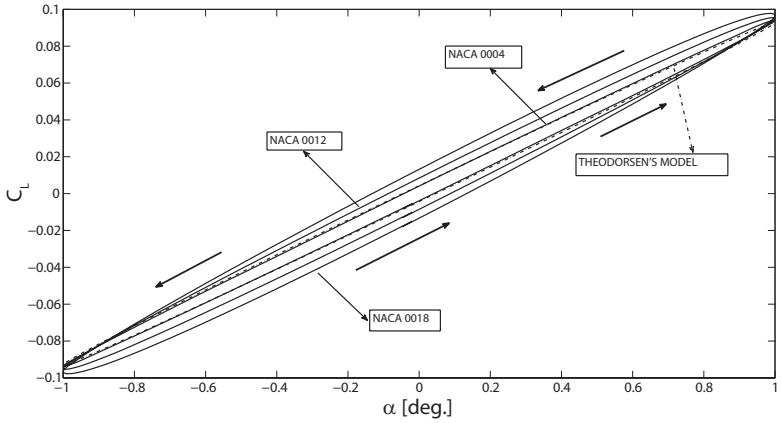

FIGURE 8. Lift coefficient hysteresis curve below the phase inversion point, $k = 0.1$.

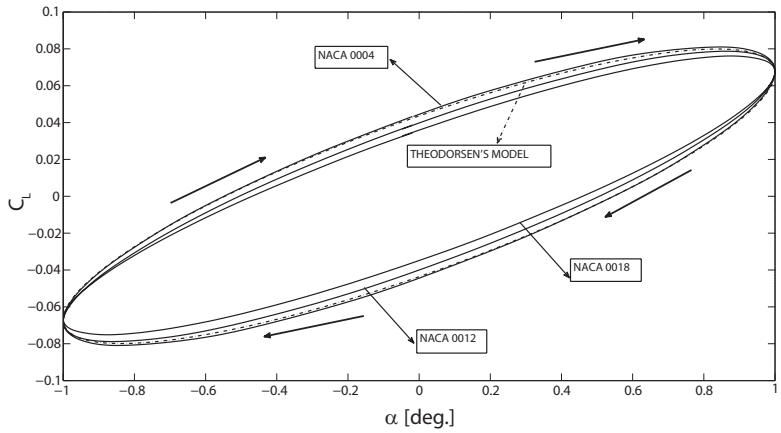

FIGURE 9. Lift coefficient hysteresis curve above the phase inversion point, $k = 0.5$.

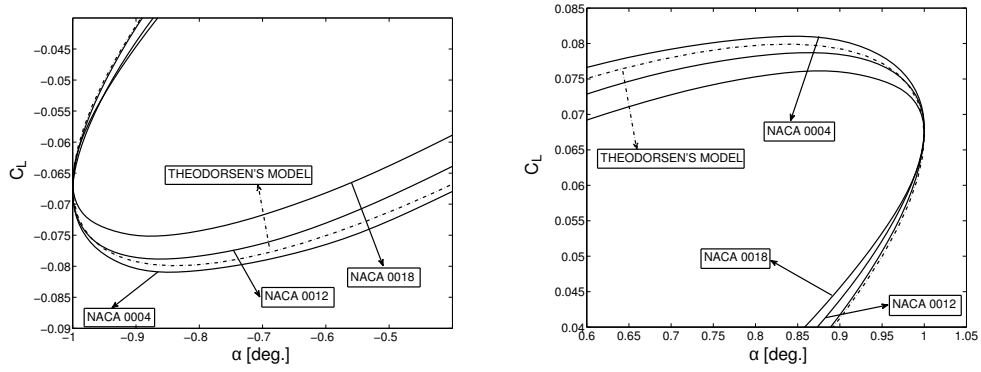

(a) Minimum (b) Maximum

FIGURE 10. Lift coefficient hysteresis curve near the minimum (left) and the maximum (right) angle of attack, $k = 0.5$.

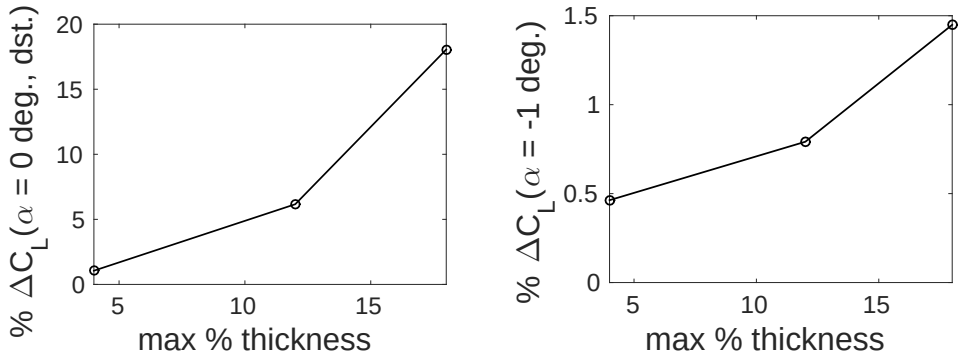

FIGURE 11. Percentage difference of lift between thick airfoils and the flat plate, evaluated at the maximum amplitude and at $\alpha = 0$ during the downstroke. The abscissa is the maximum thickness of the airfoil; $k = 0.5$.

the amplitude of the pitch motion from 1 deg. to 2 deg. In particular numerical computations were performed on a NACA 0004 and a NACA 0024 airfoil to check the linearity of the problem. Indeed it was found that both the NACA 0004 and the NACA 0024 airfoil exhibit a linear behavior (see Motta 2015). This empirically confirms that the problem can be considered linear for small amplitude oscillations, at least for maximum thickness up to 24% of the chord.

The aerodynamic behavior of thick airfoils can be explained by recalling equation (2.23), where the airfoil thickness is found to modify the unsteady contribution of the flat plate model to the boundary conditions. During the downstroke phase $d\alpha/dt > 0$, i.e. on the airfoil reference system there is an increment of the angle of attack. The last two terms of equation (2.23), featuring the same sign, are positive and therefore increase the potential difference between the upper and the lower surface. Being the last term of equation (2.23) proportional to the airfoil thickness, it results that, for thicker sections, there is a larger increase of the difference of potential and, in turn, of the developed lift. This is consistent with the behavior exhibited by the hysteresis loops in figures 8 and 9.

At the maximum and minimum angle of attack ($\alpha = \pm 1$ deg.), where $d\alpha/dt = 0$ and the thickness-related term in (2.18) is zero, the overall effect of thickness is null as shown in Figure 10 where flat-plate and thick airfoil results are almost coincident. This indicates that the main effect of thickness is due to the kinematic angle of attack rather than to the geometric angle of attack. Figure 11 shows the difference in percent between the lift coefficient of finite thickness airfoils and that of the flat plate. Such difference is evaluated both at the extremes of the oscillation cycle and at zero angle of attack, in the upstroke and in the downstroke phase. It is clearly visible, that at $\alpha = -1$ deg., the difference of lift between thick airfoils and the flat plate is at least one order of magnitude lower with respect to that visible at zero angle of attack. Additionally, this finding indicates that the main effect induced by the thickness is related to the circulatory part of the lift and not to the added mass, that is proportional to the airfoil acceleration.

For the upstroke the situation is opposite. Namely in the reference frame of the airfoil $d\alpha/dt < 0$. As a result the last two terms of equation (2.23) are negative and therefore decrease the difference of potential between the upper and the lower side. So, it results that, for thicker sections, a larger decrease in the potential difference is obtained. As a consequence, during the upstroke, the lift developed by thick airfoils is lower with respect to that generated by a flat plate. This is again consistent with the behavior exhibited by the curves in figures 8 and 9.

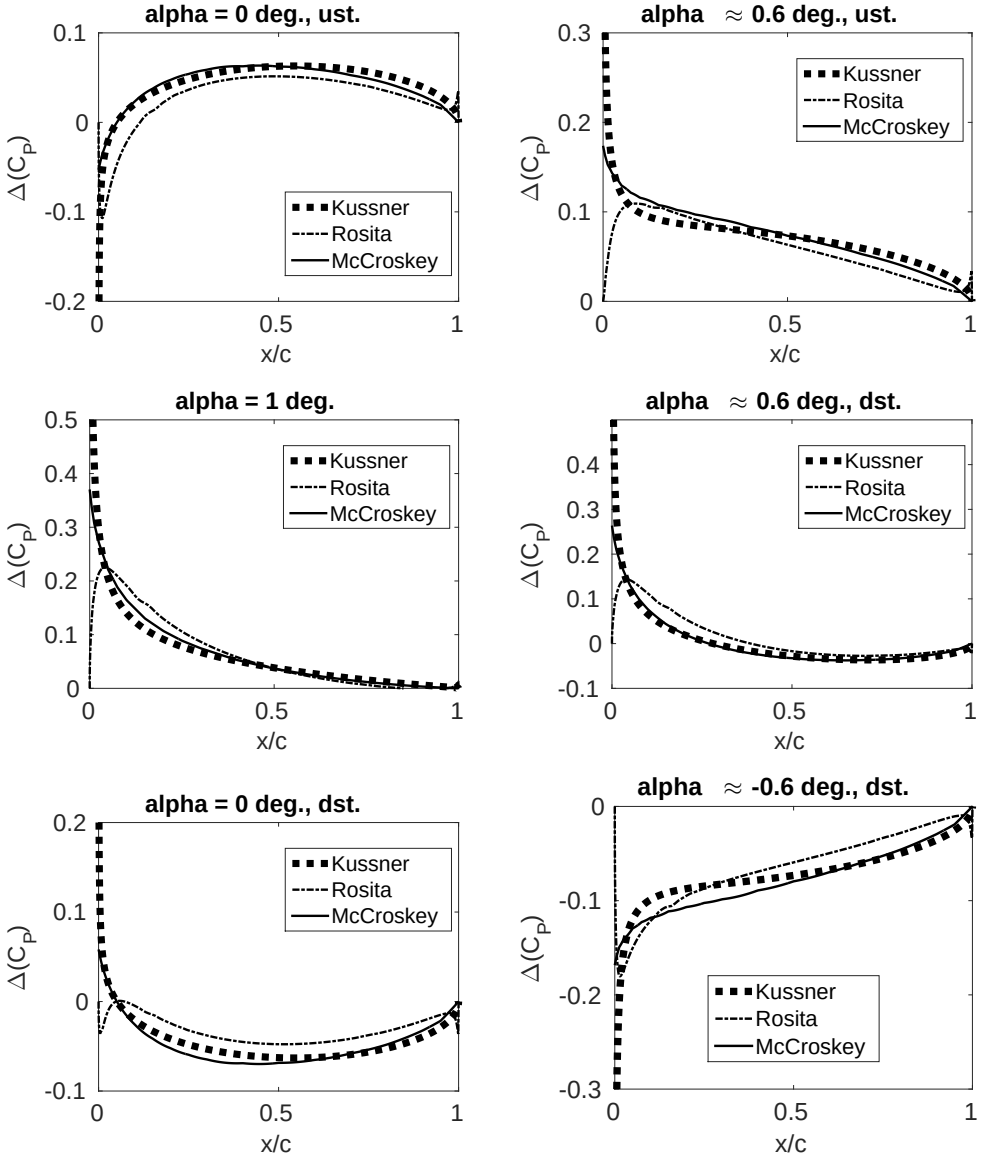

FIGURE 12. Difference of pressure coefficient between the upper and the lower side of the airfoil, for several angles of attack along the oscillation cycle. Comparison of the Küssner solution for the flat-plate with the numerical results obtained for NACA 0024 airfoil (ust: upstroke, dst: downstroke); k = 0.5, Re = 10^6, $\alpha_0 = 0$ deg., $\alpha_m = 1$ degrees.

Figure 12 shows the difference of pressure coefficient ΔC_P between the upper and the lower side, on the NACA 0024 airfoil and on the flat-plate model at different angles of attack along one oscillation cycle for a reduced frequency of $k = 0.5$, above the phase inversion condition. The C_P for the flat-plate are computed using the model developed in Küssner & Schwarz (1941). In particular, differences between the flat-plate model and the thick airfoil C_P distribution are always observed in the leading edge area, where as expected the flat-plate approximation is not applicable (see Barger 1975). However, significant differences in the C_P distribution on the upper and lower side are clearly visible

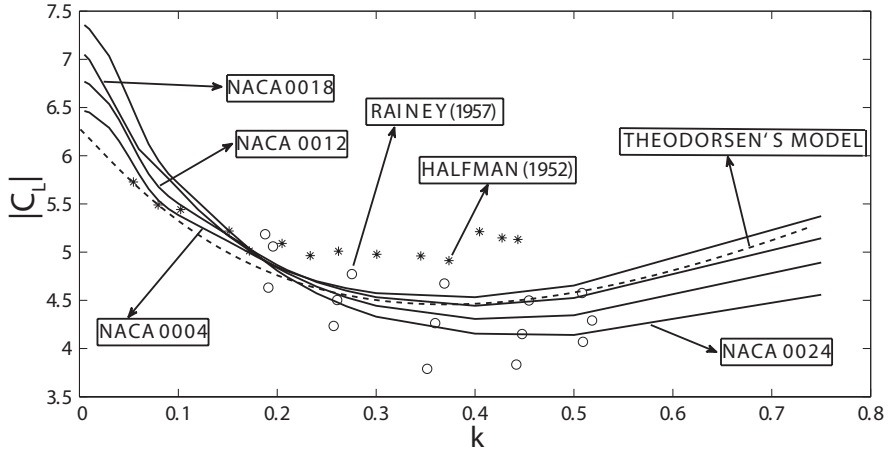

FIGURE 13. Numerical lift coefficient magnitude versus k compared to Theodorsen's model and to experimental data by Halfman (1952) and Rainey (1957).

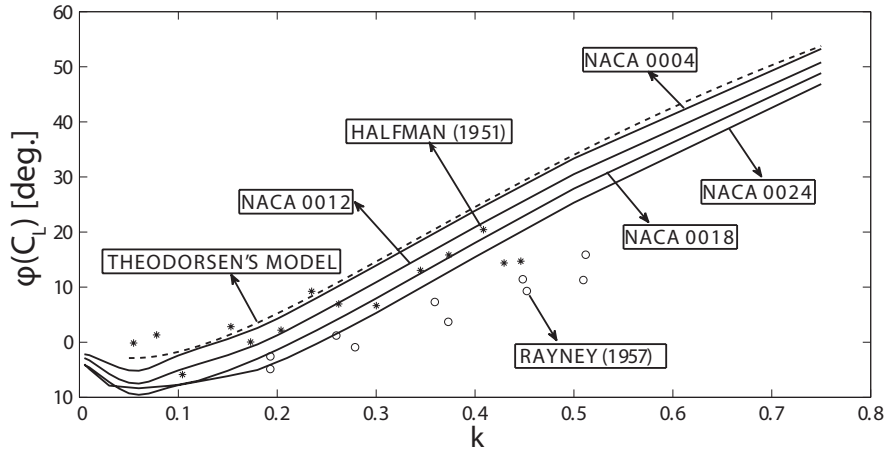

FIGURE 14. Numerical lift phase angle versus k compared to Theodorsen's model and to experimental data by Halfman (1952) and Rainey (1957).

when $\alpha = 0$ (upstroke and down-stroke), i.e. when the angular velocity is maximum, while at $\alpha = \pm 1$ deg. the difference are limited to the nose area. The differences at the trailing edge are related to the fact that, differently from the method of Küssner & Schwarz (1941) where the Kutta condition is explicitly imposed, in the CFD solver the fulfillment of the Kutta conditions, both steady and unsteady, is indirectly obtained by the introduction of the artificial viscosity in the inviscid flow equations.

Figures 13 and 14 show the effects of the thickness in terms of the amplitude and the phase of the lift coefficient transfer function. Both the amplitude and the phase retain a qualitative dependence on the reduced frequency that is similar to the flat-plate case, cd. Figures 2(a) and 2(b). However, the amplitude increases at low k by increasing the thickness and decreases at high reduced frequency, while the phase curves shift to the right, moving the phase inversion point to higher values of k as the thickness is increase. This behavior is in accordance with the observations above on the lift coefficient curve.

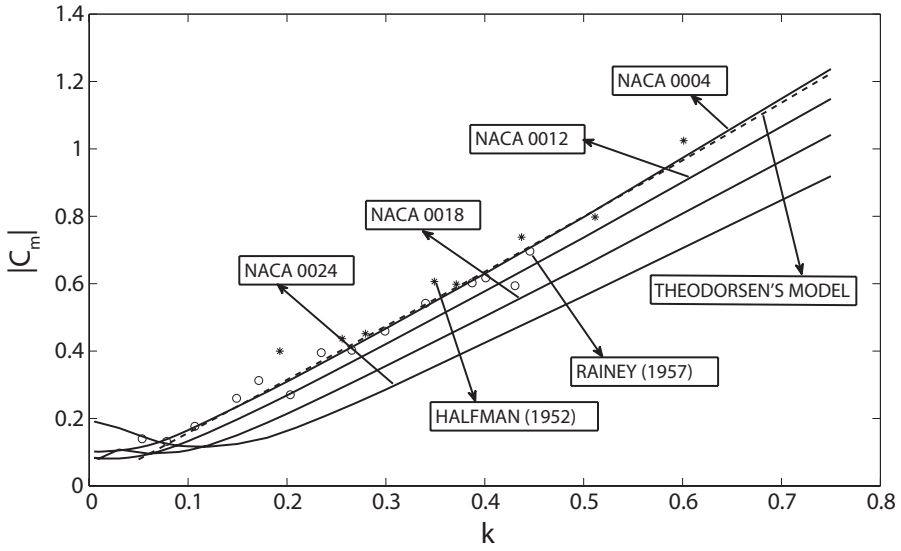

FIGURE 15. Moment coefficient magnitude versus k compared to Theodorsen's model and to experimental data.

Indeed, because of the amplification of the lift coefficient hysteresis due to thickness, phase inversion is observed at larger k. It appears also useful to gain a further insight in the behavior of the lift coefficient magnitude at $k = 0$ in Figure 13. By recalling that the lift magnitude is normalized with respect to that of the input motion (see Figure 2(a) in §2), the modulus depicted in Figure 13 evaluated at $k = 0$, is equal to the slope of the steady $C_L - \alpha$ curve. Moreover, according to the flat plate model, such value is 2π. For airfoils of larger thickness an increase in the value of the lift magnitude at $k = 0$ is observed. This is in agreement with the classical steady state aerodynamics of thick Joukowsky airfoils, where the lift coefficient slope follows the law $C_{L_\alpha} = 2\pi(1 + 0.77t/c)$, with t the maximum airfoil thickness (see for instance Currie 2012, Chapter 4). This correction is valid for small perturbations so that $\sin\alpha \sim \alpha$.

The amplitude and the phase of the moment coefficient transfer function are shown in Figures 15 and 16, together with the results from Theodorsen's theory. In this case the disagreement with respect to the Theodorsen's model can be explained by the fact that the aerodynamic center location is not at $c/4$ (a well known fact already suggested in Leishman (2006, pp.437-438)). As a consequence, the circulatory part of the lift has an influence on the moment, showing a dependency of moment coefficient on the airfoil thickness.

5. Modified Theodorsen's model for thick airfoils

The numerical experiments presented in the previous section indicate that thick airfoils exhibit a qualitatively similar behavior with respect to the flat-plate Theodorsen's model described in §2. In the present section, a simplified aerodynamic model for oscillating thick airfoils is therefore derived from the original flat-plate one. In particular, from the previous section, it can be assumed that the Theodorsen's function $C(k)$, equation(2.26), does not significantly change for thick airfoils. Therefore the new model can be obtained by scaling the formulas (2.24) and (2.25) for the lift and moment coefficient. From em-

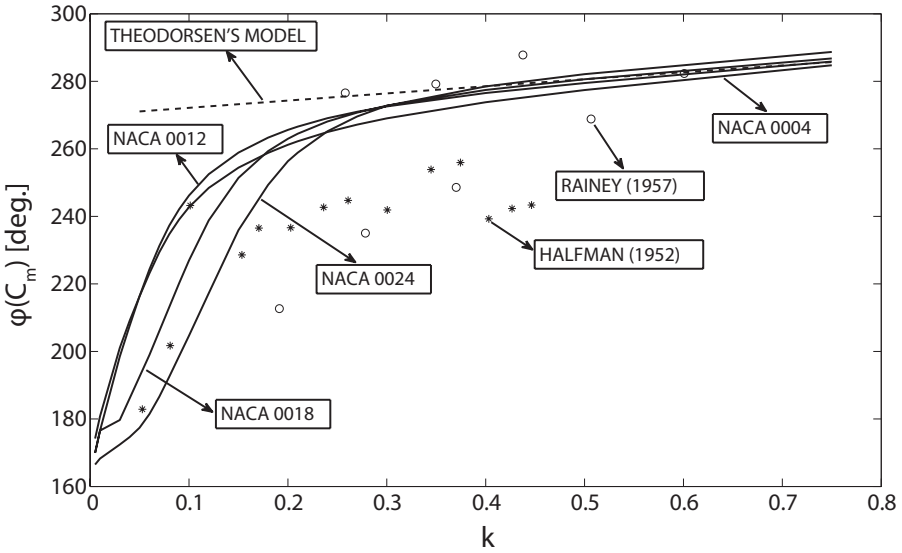

FIGURE 16. Moment coefficient phase angle versus k compared to Theodorsen's model and to experimental data.

pirical observations, the scaling factors are independent on the reduced frequency but only on the airfoil thickness.

Under these assumptions, the lift and moment frequency response functions are modeled by the following modified Theodorsen's expressions

$$C_L(k, s_m) = \pi b \left[P_1^L(s_m) \frac{\dot{\alpha}}{U} - P_2^L(s_m) \frac{ba\ddot{\alpha}}{U^2} \right] + \\ + 2\pi C(k) \left[P_3^L(s_m)\alpha + P_4^L(s_m) b \left(\frac{1}{2} - a \right) \frac{\dot{\alpha}}{U} \right], \tag{5.1}$$

$$C_m(k, s_m) = -\frac{1}{2}\pi b \left[P_1^m(s_m) \frac{1}{U}\dot{\alpha} + P_2^m(s_m) \frac{b}{2U^2} \left(\frac{1}{4} - a \right) \ddot{\alpha} \right], \tag{5.2}$$

where the maximum thickness value s_m represents the airfoil thickness. The parameters P_1^L and P_2^L and P_1^m and P_2^m, that depend on the airfoil thickness, are used to fit the added mass terms for the lift and the moment. The parameters P_3^L and P_4^L, that depend as well on the airfoil thickness, are used to fit the circulatory part of the lift. The effect on the aerodynamic moment due to the shift of the aerodynamic center is not explicitly considered, since the moment in equation (5.2) is computed around the aerodynamic center of the airfoil.

The values of the coefficients P_i^L and P_i^m for the four NACA airfoils considered in the present work are now considered. A weighted least squares fitting procedure is used to compute the values of the P coefficients, considering seventeen reduced frequencies ranging from k = 0.05 to k = 0.75. Notice that higher weights are associated to the points with higher reduced frequency, since they are affected by a smaller numerical error. The coefficients obtained are reported in table 2.

The fitting procedure is now extended to the case of an airfoil of arbitrary thickness by using an interpolation of the coefficients computed for the reference airfoils. A fourth order polynomial is used to interpolate the P_i^L and P_i^m coefficients with respect to the

TABLE 2. Fitted coefficients for the modified Theodorsen's formula (5.1) and (5.2) of the lift and moment coefficients of thick airfoils, respectively.

max thickness %	P_1^L	P_2^L	P_3^L	P_4^L	P_1^m	P_2^m
4	0.9659	1.0687	1.0111	1.0627	1.0194	0.8932
12	1.2449	0.9045	1.0393	0.7001	0.9416	0.8934
18	1.6232	0.7431	1.0623	0.2536	0.8502	0.8596
24	1.7637	0.6671	1.0567	-0.902e-2	0.7427	0.8476

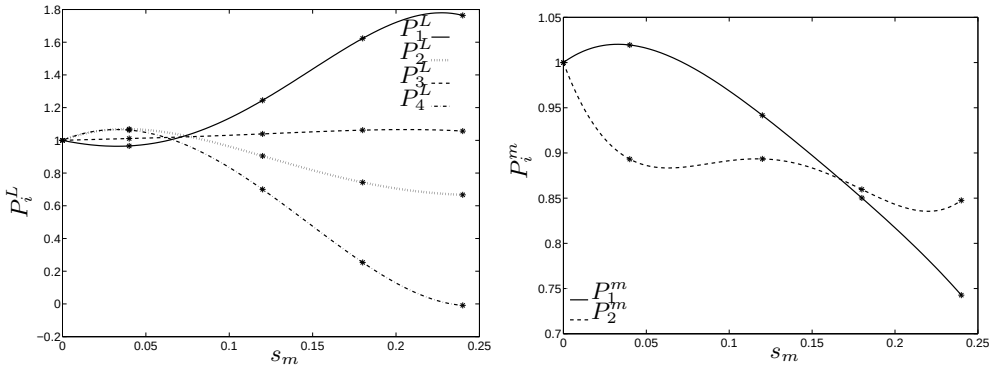

FIGURE 17. Polynomial interpolation of the coefficients versus the airfoil thickness of the modified Theodorsen's function.

maximum thickness to obtain (see figure 17)

$$P_1^L(s_m) = 1 - 2.09s_m + 25.73s_m^2 + 160.94s_m^3 - 735.68s_m^4, \tag{5.3}$$
$$P_2^L(s_m) = 1 + 3.93s_m - 64.71s_m^2 + 244.47s_m^3 - 280.08s_m^4, \tag{5.4}$$
$$P_3^L(s_m) = 1 + 0.31s_m - \ 1.65s_m^2 + \ 24.26s_m^3 - \ 77.97s_m^4, \tag{5.5}$$
$$P_4^L(s_m) = 1 + 4.17s_m - 68.51s_m^2 + \ 75.45s_m^3 + 269.26s_m^4, \tag{5.6}$$
$$P_1^m(s_m) = 1 + 1.32s_m - 24.64s_m^2 + \ 98.24s_m^3 - 154.77s_m^4, \tag{5.7}$$
$$P_2^m(s_m) = 1 - 4.92s_m + 71.09s_m^2 - 403.38s_m^3 + 756.28s_m^4. \tag{5.8}$$

To assess the validity of the obtained interpolation formulae, the symmetric NACA 0020 and the non-symmetric NACA 23012 airfoils are chosen as test cases, each of them oscillating with an amplitude of 1 degree around zero at several reduced frequencies. The NACA 23012 is selected also to test the reliability of the proposed formulation on slightly cambered airfoils.

The hysteresis curves for C_L and C_m, computed with the new formulation, are compared to the numerical results and to the classical Theodorsen's formulation. For brevity, only a case at k = 0.5 is herein reported. Figures 18 and 19, highlight better accordance of the modified models for the C_L with the numerical tests if compared with the flat plate Theodorsen's model. An increase of the accuracy can be also observed in figures 20 and 21, where the C_m hysteresis curves are reported.

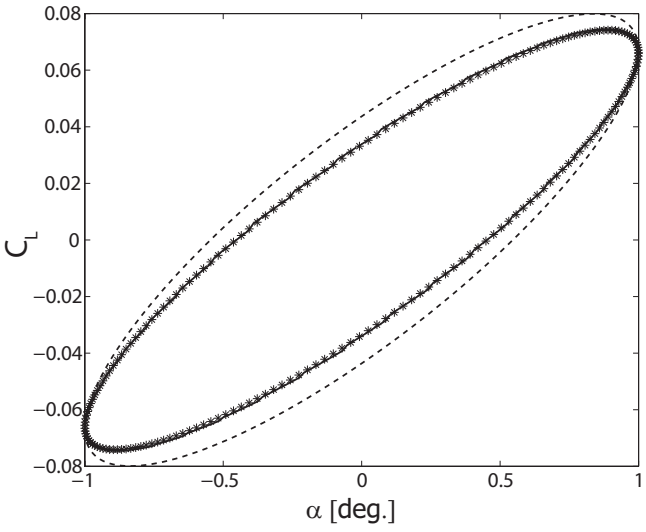

[!h]

FIGURE 18. NACA 0020 C_L hysteresis curves at k = 0.5. Stars: CFD computations; dashed line: classical Theodorsen's model; solid line: modified Theodorsen's model.

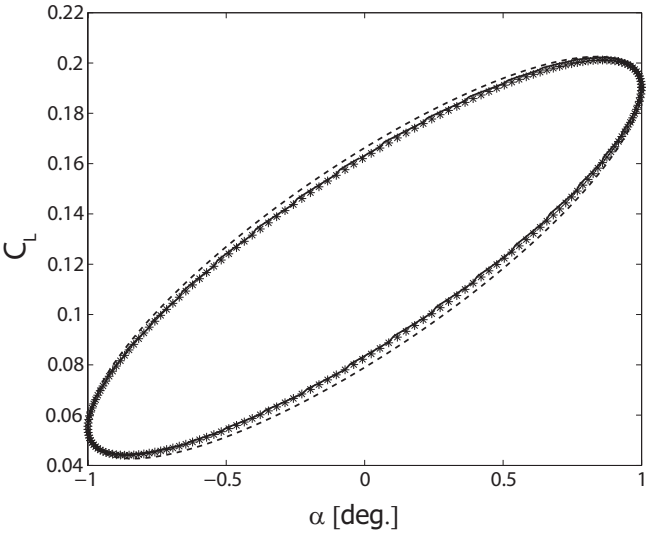

[!h]

FIGURE 19. NACA 23012 C_L hysteresis curves at k = 0.5. Stars: CFD computations; dashed line: classical Theodorsen's model; solid line: modified Theodorsen's model.

5.1. *Applicability of the modified Theodorsens model to viscous flows*

The modified Theodorsen model devised in the previous section was identified by neglecting the effect of the viscosity, since unsteady flows without major separation were considered. In section 3 it was shown through a comparison with experimental data how the not-separated model remains valid also for large oscillations, for the NACA 0012 up to 6 deg. of oscillation as shown in figure 3(a). Additionally, it was shown that the effects of viscosity are negligible for the NACA 0012.

Since the modified Theodorsen's model proposed in the previous section extends to

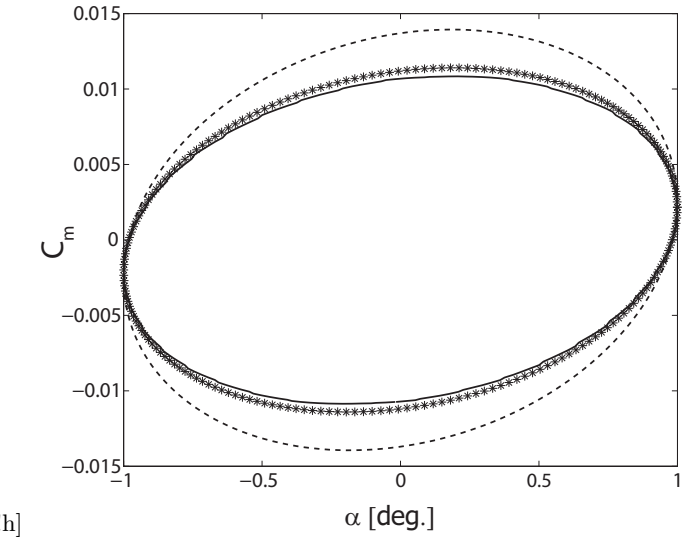

[!h]

FIGURE 20. NACA 0020 C_m hysteresis curves at k = 0.5. Stars: CFD computations; dashed line: classical Theodorsen's model; solid line: modified Theodorsen's model.

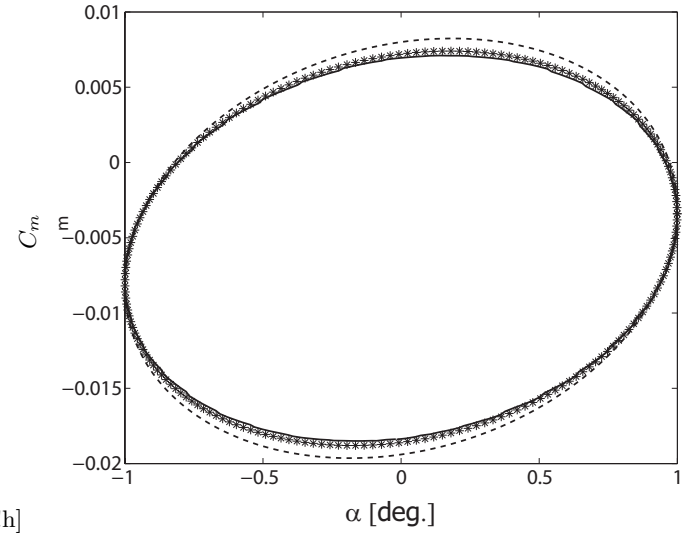

[!h]

FIGURE 21. NACA 23012 C_m hysteresis curves at k = 0.5. Stars: CFD computations; dashed line: classical Theodorsen's model; solid line: modified Theodorsen's model.

airfoil thickness up to 24%, it is important to check if the hypothesis of low relevance of the viscosity up to this thickness is still valid. For this reason several numerical tests were performed with a pitch amplitude of 1 deg. using a RANS viscous models at a reduced frequency of k = 0.5 with the NACA 0018, 0020 and 0024 airfoils. The Spalart & Allmaras (1994) turbulence model is used for viscous computations, which are performed

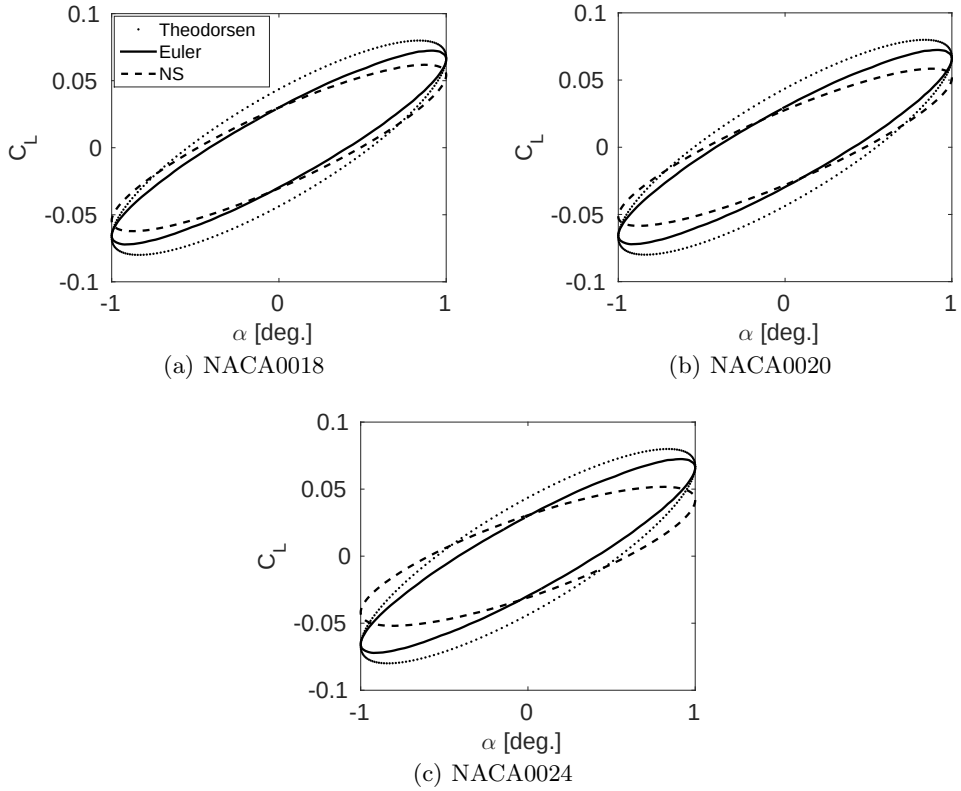

(a) NACA0018 (b) NACA0020

(c) NACA0024

FIGURE 22. Comparison of the hysteresis curve obtained by inviscid and viscous ($\mathrm{Re} = 10^6$) CFD models at $\mathrm{k} = 0.5$ with the flat-plate Theodorsen's model results.

at a Reynolds number of one million. The comparison of the hysteresis cycles obtained with and without viscosity are shown in figure 22.

Figure 22 shows that the modification of the hysteresis cycle due the viscosity for attached flow on thick airfoils is less significant than the effect due to the thickness in inviscid flows up to airfoils thicknesses of 18%. Over 18% the modification due to viscosity becomes significant. The inclusion of viscosity cause a modification of the slope of the hysteresis cycle only, without affecting the amplitude of the cycle. On the contrary, from the present simulations the inclusion of thickness in an inviscid flow was shown to lead to a change of the amplitude of the hysteresis cycles.

It is possible to speculate that this modification of the slope of the hysteresis due to viscosity may be caused by a shift downstream of the location of the point where the Kutta condition must be enforced, in a similar fashion to what happens for airfoils equipped with Gurney flaps (see Liebeck 1978; Motta & Quaranta 2015). In fact for thick airfoils, the thickness of the boundary layer at the trailing edge becomes significant, and a small recirculation region appears behind the trailing edge. The shift downstream of the Kutta condition causes an increase of the equivalent chord of the airfoil, which in turns leads to a increase of the apparent reduced frequency. This increase of apparent reduced frequency may explain the change of slope, since there is a direct dependency between the increase of slope of the hysteresis cycle and the increase of reduced frequency, as shown in (Leishman 2006, pp. 434–436). A detailed investigation of these effects is beyond the

scope of this work, however it is possible to affirm that the inclusion of the viscosity leads to further modifications of the loads that are significant only above a thickness of 18%. Moreover, the effect of viscosity can be accounted for by fine tuning the modified Theodorsen's model here presented. In any case, given the nature of the modification of the cycle induced by the viscosity, it not expected to find a significant modification of the inversion reduced frequency due to viscosity.

In conclusion, it is possible to state that the presented correction model should be considered valid up to a thickness of 18%, and somehow still valid up to a thickness 24%, at least for what regards the amplitude of the hysteresis cycle. For airfoils with thickness above 18%, an additional effect due to viscosity on the slope of the hysteresis should be considered.

6. Conclusions

The effects of the airfoil thickness on the aerodynamic loads generated by an harmonic motion were investigated numerically. As expected from a detailed analysis of the boundary conditions, a dependency of the linearized lift and moment coefficient on the thickness was studied for the case of pitch movements.

Numerical results obtained using the flow solver ROSITA showed a dependency of the loads on the thickness. In particular, the inversion reduced frequency—at which the phase inversion of the lift-coefficient curve occurs—depends on the thickness of the airfoil. The amplitude of the lift hysteresis cycle is larger for thicker airfoils, for reduced frequencies below the inversion frequency, and smaller for reduced frequencies above it. This modification results in a shift of the phase inversion point towards higher reduced frequencies for thicker airfoils.

A fitting procedure was applied to identify a modified Theodorsen's linear model that accounts for the airfoil thickness. The flat-plate Theodorsen's model was used as a starting point. The resulting simplified model was found to accurately predict the unsteady lift and moment coefficients for symmetric and slightly cambered airfoils of arbitrary thickness, from 4% to 24%, in the considered range of reduced frequencies under the assumptions of the small-perturbation theory. Additional modifications due to viscosity, and related to the slope of the hysteresis cycle, have been identified for airfoils with a thickness above 18%.

REFERENCES

Abbott, I.H. & von Doenhoff, A.E. 1949 *Theory of Wing sections*. New York, NY: Dover Publication, Inc.

Anderson, JM, Streitlien, K, Barrett, DS & Triantafyllou, MS 1998 Oscillating foils of high propulsive efficiency. *Journal of Fluid Mechanics* **360** (1), 41–72.

Archibald, FS 1975 Unsteady kutta condition at high values of the reduced frequency parameter. *Journal of Aircraft* **12** (6), 545–550.

Baik, Yeon Sik, Bernal, Luis P, Granlund, Kenneth & Ol, Michael V 2012 Unsteady force generation and vortex dynamics of pitching and plunging aerofoils. *Journal of Fluid Mechanics* **709**, 37–68.

Barger, R.L. 1975 Adaptation of the Theodorsen Theory to the Representation of an Airfoil as a combination of a Lifting Line and a Thickness Distribution. TN D-8117. NASA.

Biava, M. 2007 RANS computations of rotor/fuselage unsteady interactional aerodynamics. PhD thesis, Politecnico di Milano.

Bisplinghoff, R.L., Ashley, H. & Halfman, R.L. 1955 *Aeroelasticity*. Cambridge, Mass.: Addison–Wesley Publishing Company.

Bohl, Douglas G & Koochesfahani, Manoochehr M 2009 Mtv measurements of the vortical field in the wake of an airfoil oscillating at high reduced frequency. *Journal of Fluid Mechanics* **620**, 63–88.

Cicala, P. 1936 Le azioni aerodinamiche sul profilo oscillante. *L'Aerotecnica* **16**, 652–655.

Currie, I.G. 2012 *Fundamental Mechanics of Fluids, Fourth Edition*. Boca Raton, FL: CRC Press.

Drikakis, D., Zhong, B., Barakos, G., Steijl, R., Biava, M., Vigevano, L., Brocklehurst, A., Boelens, O.J., Dietz, M., Embacher, M., Khier, W. & Antoniadis, A.F. 2012 Methods Against Experimental Flow Measurements for Helicopter Flows. *Aerospace Science and Technology* **19** (1), 86–100.

Freymuth, P. 1988 Propulsive vortical signature of plunging and pitching airfoils. *AIAA journal* **26** (7), 881–883.

Fung, Y.C. 1955 *Theory of Aeroelasticity*. New York: John Wiley and Sons, Inc.

Garrick, I.E. 1936 Propulsion of a Flapping and Oscillating Airfoil. TR 567. NACA.

Garrick, I.E. 1938 On Some Reciprocal Relations in the Theory of Nonstationary Flows. TR 629. NACA.

Gennaretti, M., Testa, C. & Bernardini, G. 2013 An unsteady aerodynamic formulation for efficient rotor tonal noise prediction. *Journal of Sound and Vibration* **332** (25), 6743–6754.

Glegg, S. A.L. & Davenport, W. 2009 Unsteady loading on an airfoil of arbitrary thickness. *Journal of Sound and Vibration* **319**.

Goldstein, M. E. & Atassi, H. 1976 A complete second-order theory for the unsteady flow about an airfoil due to a periodic gust. *Journal of Fluid Mechanics* **74**, 741–765.

Halfman, R.L. 1952 Experimental aerodynamic derivatives of a sinusoidally oscillating airfoil in two-dimensional flow. TR 1108. NACA.

Jameson, A, Schmidt, W & Turkel, E 1981 Numerical Solution of the Euler Equations by Finite Volume Methods Schemes. In *14th AIAA Fluid and Plasma Dynamic Conference*.

Johnson, W. 1980 *Helicopter Theory*. Princeton University Press.

Katz, J. & Plotkin, A. 1991 *Low-speed aerodynamics: from wing theory to panel methods*. New York, NY: McGraw-Hill.

Khier, W., Vigevano, L. & Biava, M. 2012 Prediction of Air Flow Past a Full Helicopter Configuration. *Aerospace Science and Technology* **19** (1), 3–18.

Kinzel, M.P., Maughmer, M.D. & Duque, E.P. 2010 Numerical Investigation on the Aerodynamics of Oscillating Airfoils with Deployable Gurney Flaps. *AIAA Journal* **48** (7), 1457–1469.

Kurosaka, M 1974 On the flow field of a rapidly oscillating airfoil in a supersonic flow. *Journal of Fluid Mechanics* **62** (04), 811–827.

Küssner, H.G. 1936 Zusammenfassender Bericht über den instationären Auftrieb von Flügeln. *Luftfahrtforschung* **13** (12), 410–424.

Küssner, H.G. 1960 Nonstationary theory of airfoils of finite thickness in incompressible flow. In *AGARD Manual on aeroelasticity. Part 2* (ed. W.P. Jones), chap. 8.

Küssner, H.G. & Schwarz, L. 1941 The oscillating wing with aerodynamically balanced elevator. TM 991. NACA, translated from Luftfahrtforschung, vol. 17, pp. 337–354, 1940.

Lee, T & Gerontakos, P 2004 Investigation of flow over an oscillating airfoil. *Journal of Fluid Mechanics* **512**, 313–341.

Leishman, J. G. 2006 *Principles of Helicopter Aerodynamics*. Cambridge University Press, 2nd edition.

Liebeck, R. H. 1978 Design of Subsonic Airfoils for High Lift. *Journal of Aircaft* **15** (9), 547–561.

Lin, P.T., Baker, T.J., Martinelli, L. & Jameson, A. 2006 Two-dimensional implicit time-dependent calculations on adaptive unstructured meshes with time evolving boundaries. *International journal for numerical methods in fluids* **50** (2), 199–218.

McCroskey, W.J. 1973 Inviscid Flowfield of an Unsteady Airfoil. *AIAA Journal* **11** (8).

McCroskey, WJ 1982 Unsteady airfoils. *Annual Review of Fluid Mechanics* **14** (1), 285–311.

Morino, L. 1974 A General Theory of Compressible Potential Aerodynamics. CR 2464. NASA.

Morino, L. 2003 Is There a Difference Between Aeroacoustics and Aerodynamics? An Aeroelastician's Viewpoint. *AIAA Journal* **41** (7), 1209–1223.

Morino, L., Chen, L. T. & Suciu, E. O. 1975 Steady and Oscillatory Subsonic and Supersonic Aerodynamics Around Complex Configurations. *AIAA Journal* **13** (3), 368–374.

Motta, V. 2015 Computational fluid dynamic analysis of a L-shaped Gurney flap for vibration control. PhD thesis, Politecnico di Milano.

Motta, V. & Quaranta, G. 2015 Linear reduced-order model for unsteady aerodynamics of an L-shaped Gurney flap. *Journal of Aircraft* Accepted for publication.

Panda, J & Zaman, KBMQ 1994 Experimental investigation of the flow field of an oscillating airfoil and estimation of lift from wake surveys. *Journal of Fluid Mechanics* **265**, 65–95.

Rainey, A.G. 1957 Measurement of aerodynamic forces for various mean angles of attack on an airfoil oscillating in pitch and on two finite-span wings oscillating in bending with enphasis on damping in the stall. Report 1305. NACA.

Roe, P L 1981 Approximate Riemann solvers, parameter vectors, and difference schemes. *J. Comput. Phys.* **43**, 357–372.

Spalart, P R & Allmaras, S R 1994 A one-equation turbulence model for aerodynamic flows. *La Recerche Aérospatiale* **1**, 5–21.

Theodorsen, T. 1931 Theory of Wing Sections of Arbitrary Shape. *Tech. Rep.*. Langley Memorial Aeronautical Laboratory.

Theodorsen, T. 1935 General Theory of Aerodynamic Instability and the Mechanism of Flutter. TR 496. NACA.

Uldrick, JP & Siekmann, J 1964 On the swimming of a flexible plate of arbitrary finite thickness. *Journal of Fluid Mechanics* **20** (01), 1–33.

Van Dyke, M.D. 1953 On second-order supersonic flow past a slowly oscillating airfoil. *Journal of the Aeronautical Sciences (Institute of the Aeronautical Sciences)* **20** (1), 61.

Venkatakrishnan, V. & Mavriplis, D.J. 1996 Implicit method for the computation of unsteady flows on unstructured grids. *Journal of Computational Physics* **127** (2), 380–397.

VV. AA. 1982 Compendium of unsteady aerodynamic measurements. Report no. 702. AGARD.

Wagner, H. 1925 Über die Entstehung des dynamischen Auftriebes von Tragflügeln. *Zeitschrift für Angewandte Mathematik und Mechanik* **5** (1), 17–35.